JGR Planets

RESEARCH ARTICLE
10.1029/2018JE005796

Key Points:
- McLaughlin crater contained a deep, voluminous lake >3.8 Ga with features unlike any other known Martian paleolakes
- Sedimentary units include delta deposits, turbidites, and deep-water sediments; and hydrothermal deposits include serpentinites
- Geochemical gradients occurred in a long-lived lake that was in sustained communication with groundwater and subsurface environments

Correspondence to:
J. R. Michalski,
jmichal@hku.hk

Citation:
Michalski, J. R., Glotch, T. D., Rogers, A. D., Niles, P. B., Cuadros, J., Ashley, J. W., & Johnson, S. S. (2019). The geology and astrobiology of McLaughlin crater, Mars: An ancient lacustrine basin containing turbidites, mudstones, and serpentinites. *Journal of Geophysical Research: Planets*, *124*, 910–940. https://doi.org/10.1029/2018JE005796

Received 15 AUG 2018
Accepted 7 JAN 2019
Accepted article online 15 JAN 2019
Published online 8 APR 2019

The Geology and Astrobiology of McLaughlin Crater, Mars: An Ancient Lacustrine Basin Containing Turbidites, Mudstones, and Serpentinites

Joseph R. Michalski[1,2,3], T. D. Glotch[4], A. Deanne Rogers[4], Paul B. Niles[5], J. Cuadros[3], James W. Ashley[6], and Sarah Stewart Johnson[7]

[1]Department of Earth Sciences, University of Hong Kong, Hong Kong, [2]Laboratory for Space Research, University of Hong Kong, Hong Kong, [3]Natural History Museum, London, UK, [4]Department of Geosciences, Stony Brook University, Stony Brook, NY, USA, [5]NASA Johnson Space Center, Houston, TX, USA, [6]Jet Propulsion Laboratory, Pasadena, CA, USA, [7]Department of Biology, Georgetown University, Washington, DC, USA

Abstract McLaughlin crater is a 92-km diameter complex crater that formed on Mars ~4 billion years ago. The resulting basin was the site of a large (~3,000 km^2), deep (~500 m), voluminous (~1,500 km^3) Martian lake circa 3.8 Ga. While there is strong evidence that hundreds of lakes have existed on Mars at some point during the same time period, the geology of McLaughlin crater is extraordinary for a number of reasons. Detailed spectral analyses show that the deep-water sediments include detrital inputs of olivine and pyroxene, but the lake-floor sediments include lithologies with abundant Fe-rich, Mg-bearing smectite, serpentine-rich deposits, and ferrihydrite. For astrobiologists, this site provides a treasure trove of high-priority targets. Serpentinization reactions are thought to have played a key role in abiogenesis on Earth, and within McLaughlin crater, deposits of subterranean and probably sublacustrine serpentinites are well preserved. In addition, delta sequences are well exposed throughout the east side of the basin; such deposits are endorsed by some as the highest priority targets for preservation of organics on Mars. Yet deep-water turbidites, which might have flowed through hydrothermal environments, may be the most intriguing aspect of this geology. Such rapid sedimentation could have sequestered and preserved any potential organic materials for future exploration by a rover.

Plain Language Summary Though Mars is cold, dry, and inhospitable today, it contains evidence for many dry lake beds—relics of an ancient climate that was at least episodically warmer and wetter. Considering that lakes can be an excellent environments for life on Earth, a common thread of Mars research has been to characterize the environmental conditions under which Martian lakes formed in order to better understand their implications for past habitability of the red planet. The goal of this work is to characterize the geology of McLaughlin crater, where a lake existed on Mars over 3.8 billion years ago. McLaughlin lake was vast, deep (~ 500 m), and probably long lived. Many characteristics of McLaughlin lake are unlike those seen in any other ancient lake basins on Mars. This lake contained a range of sedimentary environments including delta deposits, shallow-water fan deposits, and deep-water, fine-grained materials. It is the only known place on Mars where fine-grained, subaqueous "landslides" called turbidites are identified, and these are important because we know that such deposits can be sites of excellent preservation of organic matter on Earth (due to rapid burial).

1. Introduction

Over four decades ago, the first global remote sensing survey of Mars revealed clues that possible lacustrine basins might have existed within an ancient, cratered landscape (Carr & Clow, 1981) More recent data have shown topographic and geomorphological evidence for many lacustrine environments on Mars (Achille & Hynek, 2010), and we now have confirmation that several hundred lakes existed, at least for short periods, in the Noachian (estimated at 3.6–4.1 Ga, Carr & Head, 2010).

Most ancient lacustrine basins on Mars are identified by the relationship between fluvial features and the topography that defines the basins (Fassett & Head, 2008). While ancient open-basin lakes are fairly straightforward to identify on Mars from their association with inflowing and outflowing channels, closed-basin lakes can be more difficult to detect and assess because they contain only an inlet valley (Goudge et al., 2015). Without an outflowing channel, it is difficult to determine the height of an ancient lake level and

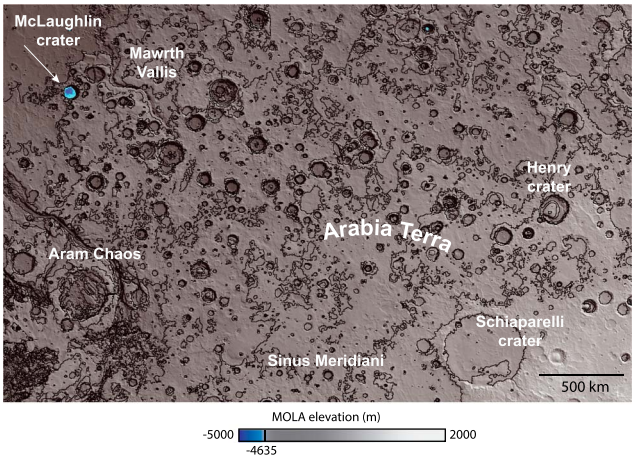

Figure 1. MOLA elevation data are shown for western Arabia Terra. Contours are shown at 1,000-m intervals. The data are colorized such that elevations below −4,635-m elevation are shown in blue, and all elevations above this level are shown in grayscale. The significance of the −4,635-m level is described in the text and illustrated in Figure 2. MOLA = Mars Orbiter Laser Altimeter.

therefore difficult to definitively prove that a lake existed. However, suites of observed geomorphological features (channels, deltas, layered basin materials, etc.) can provide strong evidence that water gathered in a given basin for some duration (Goudge et al., 2018). Such geomorphological evidence is in some cases corroborated by infrared evidence for minerals consistent with lacustrine deposits (clay minerals, sulfates, chlorides, etc.; Ehlmann, Mustard, Fassett, et al., 2008; Wray et al., 2011).

While a focus on fluvio-lacustrine systems is sensible, this approach cannot detect underfilled, lacustrine basins that are not associated with external channels and such spring-fed lakes might be among the most interesting sites in terms of astrobiological potential due to their connection with protected subsurface environments (Michalski et al., 2018). McLaughlin crater is a possible example of such a site. This large impact crater, located just to the south of the dichotomy boundary in northwest Arabia Terra, is one of the deepest basins for thousands of kilometers in any direction. Given the predicted northward flow of deep groundwater on Mars (Andrews-Hanna et al., 2010), this site would be a likely location for a spring-fed lake to occur (Figure 1).

The idea that McLaughlin crater once contained a deep, ancient lake was originally proposed by Michalski et al. (2013). That initial paper only described some of the arguments for a lacustrine environment based on early observations and data available at that time. Here we fully document the evidence for an ancient lake in McLaughlin crater, describe the morphological and mineralogical features associated with lacustrine deposits, interpret the geologic setting, and consider the astrobiological potential of such an environment.

2. Methods

The geology of McLaughlin crater was studied primarily using remote sensing data from the following missions: Mars Global Surveyor (MGS), Mars Odyssey (MO), Mars Express (MEx), and Mars Reconnaissance Orbiter (MRO). Data were obtained and organized using the Java Mission-planning and Analysis for Remote Sensing software developed and operated by Arizona State University (Christensen et al., 2009).

2.1. Topography, Geomorphology and Thermophysics

Topography of McLaughlin crater was analyzed using four data sets. MGS Mars Orbiter Laser Altimeter (MOLA) data available in gridded (463 m/pixel) format provide a regional context. Digital elevation models (DEMs) derived from stereo imaging by the MEx High-Resolution Stereo Camera (HRSC) produced by the Freie Universitaet and the German Aerospace Center (DLR) provide mesoscale elevation data at ~50 m/pixel. Higher-resolution topographic data were analyzed using stereo images from the MRO Mars Context Imager (CTX), converted to a 20-m/pixel DEM by the Mars 2020 Entry Descent and Landing team at the Jet Propulsion Laboratory, and stereo images from the MRO High-Resolution Imaging Science Experiment (HiRISE) instrument at 1 m/pixel. Note that the high-resolution DEM data from HiRISE and CTX are currently only available for a portion of the crater. Topographic data were also converted to slope measurements in order to evaluate steepness of terrain.

Geomorphology was evaluated using visible and thermal infrared images. Thermal infrared data from the MO Thermal Emission Imaging System (THEMIS) available in a global 100-m/pixel mosaic available in Java Mission-planning and Analysis for Remote Sensing provide a mesoscale base map (Edwards et al., 2011). Visible images used include higher-resolution data available from HRSC at 10–20 m/pixel, CTX at ~6 m/pixel, and HiRISE at ~0.25 m/pixel. Data were obtained in radiometrically corrected and geometrically projected format and ingested into a geographic information system for analysis and interpretation. Visible images were draped over digital topography in order to create 3D views of bedding and surface morphology.

Thermophysical properties were evaluated using THEMIS and MGS Thermal Emission Spectrometer (TES) data. The TES data were previously processed into a global thermal inertia data set (Christensen et al., 2001),

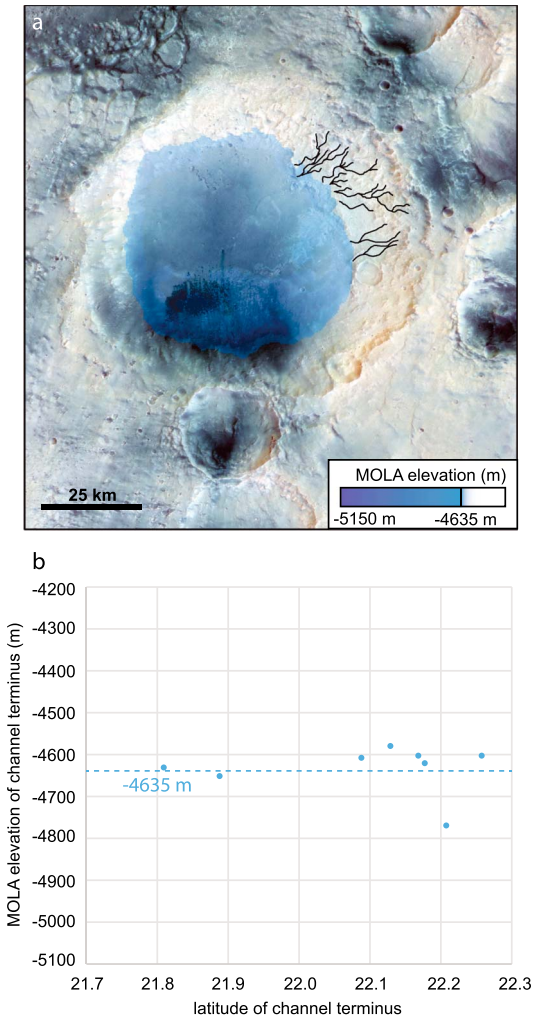

Figure 2. (a) HRSC color data. Colorized HRSC digital elevations are draped over the image data, where the elevations above −4,635-m elevation are omitted and elevations below this elevation are shown in blue colors. Fluvial channels were mapped in the eastern part of the basin. (b) The elevation at which each channel network terminates extracted from the DEM data as a function of latitude of the channel termini. The average terminus elevation is −4,635 m, which we interpret as a base level of an ancient lake at the time when the channels were active. HRSC image H1564_0008. MOLA = Mars Orbiter Laser Altimeter; HRSC = High-Resolution Stereo Camera; DEM = digital elevation model.

though at relatively coarse spatial resolution (8 pixels per degree). Despite the coarse spatial resolution, these data provide a stable and reliable measure of thermal inertia (J $m^{-2}{\cdot}K^{-1}{\cdot}s^{-1/2}$). THEMIS thermal inertia data were used to investigate the thermophysical properties of the surface at higher spatial resolution (100 m/pixel, Christensen et al., 2013). While TI values do not translate directly to quantified estimates of particle size or induration, higher values translate to surfaces with coarser grains, rocky materials, better indurated materials, or some combination of all three of these scenarios.

2.2. Surface Composition

Surface mineralogy was investigated using near-infrared reflectance and thermal emission data. The TES instrument measured thermal radiance between ~6 and 50 μm and has a spatial sampling of ~ 3 × 8 km. TES emissivity spectra were extracted from the TES database using the warm surface temperature and data quality constraints of Rogers and Christensen (2007) and corrected for atmospheric aerosol contributions using the linear least squares unmixing method described by (Bandfield, 2002; Smith et al., 2000). A spectral library of basaltic minerals and secondary minerals, along with atmospheric components, was used to fit each spectrum. The atmospheric components were then scaled by their modeled abundances and subtracted to produce surface emissivity. THEMIS daytime IR radiance data were also used to investigate spectral variability within the study region. Radiance images were processed using a decorrelation stretch method, which emphasizes spectral radiance differences attributable to compositional variation (Gillespie et al., 1986).

Near-infrared data from the MEx *Observatoire pour la Minéralogie, l'Eau, les Glaces et l'Activité* (OMEGA) and the MRO Compact Reconnaissance Imaging Spectrometer for Mars (CRISM) were processed to correct for instrument effects and minimize atmospheric absorptions using a standard data analysis pipeline (Bibring et al., 2005; Murchie et al., 2007). Both data sets rely on the use of an atmospheric transmission spectrum scaled by elevation (path length) with atmospheric effects estimated for a given Martian L_s. As a result, (due to the estimated rather than measured atmospheric properties) there are usually some residual atmospheric effects even in the corrected spectra. These can be minimized by using spectral ratios, which divide a spectrum of interest (numerator) by a spectrum from the same scene over a spectrally unremarkable terrain of comparable albedo (denominator, Mustard et al., 2008; Poulet et al., 2005). This technique has the advantage of emphasizing unique spectral features related to a certain surface of interest (usually mineralogical absorptions of interest), but it has the disadvantage of converting the spectra from units of I/F (which is comparable to radiance) into unitless spectra, comparable in shape to laboratory spectra but not comparable in absolute units.

We analyzed all CRISM images targeted within McLaughlin crater. Our analyses focused primarily on CRISM observations corresponding to full resolution targeted images (18 m/pixel), with some half resolution long images (36 m/pixel) and half resolution short images. Some of the images used in this work were acquired by CRISM after 2012, when one of the cryocoolers failed. As a result of this normal system decay, data collected after that date contain more noise than data collected before the cooler failed. Images collected in the newer observing mode are called full resolution short (FRS).

CRISM I/F images were also converted to spectral summary products. These data products were created using the CAT_ENVI software package using combinations of spectral ratios tuned for sensitivity to

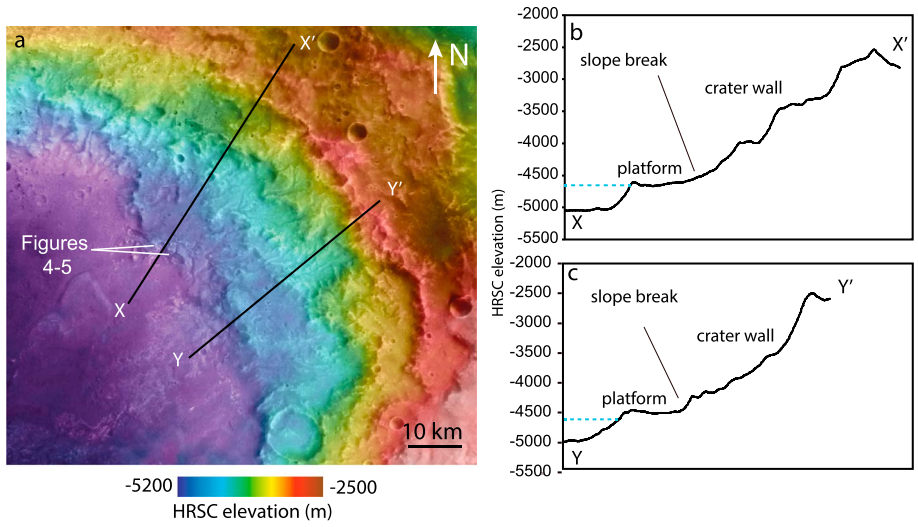

Figure 3. (a) HRSC DEM data draped over HRSC image data. A broad topographic platform is present at elevations between approximately −4,500 and −4,700 m. (b and c) Topographic profiles through this platform are shown at the right. Note the steep slope corresponding to the crater wall in the northeast and the break in slope associated with the platform. HRSC image H1337_0009. HRSC = High-Resolution Stereo Camera; DEM = digital elevation model.

various minerals or mineral groups (Viviano-Beck et al., 2014). Such maps are useful for evaluating the likely presence of a particular mineral and for mapping relative signal strength corresponding to the unique features associated with that mineral, but these maps do not correspond to actual mineral abundances and they require verification in order to validate mineral occurrences.

Estimates of actual mineral abundances were derived using two methods, one for near IR data and one for thermal IR data. Two CRISM images, FRTA5AA and FRTA27C, were atmospherically corrected using the Discrete Ordinates Radiative Transfer (DISORT) radiative transfer code (Stamnes et al., 2000) according to the methods of Liu et al. (2016). DISORT is a multilayer radiative transfer model in which the scattering properties of each layer are constant but can vary between layers. The lower boundary is the Martian surface described by a Hapke model (Hapke, 1999) with parameters defined by Wolff et al. (2009). Inputs into the model include dust and ice aerosol optical depths; dust single-scattering albedo and phase function; CO, CO_2, and water vapor abundances; atmospheric temperature and pressure profiles; and CRISM viewing geometry. On a channel-by-channel basis, the model calculates I/F and uses a lookup table to replace I/F with surface single-scattering albedos.

Because single-scattering albedos add linearly, a linear spectral mixture analysis model can be used to calculate mineral abundances. Inputs into the linear spectral mixture analysis model include mineral optical constants and possible grain sizes. The model, described in Liu et al. (2016) returns areal fractions of minerals and particle size(s) associated with each mineral. Unmixing spectra of laboratory mixtures indicate that mineral abundances can be determined to within 5% of known values (Robertson et al., 2016). Unmixing orbital spectra of more complex assemblages will likely result in larger errors, which we estimate to be on the order of 10–15% volume abundance per phase, similar to errors associated with unmixing of thermal infrared emission spectra.

TES surface emissivity spectra were modeled using a spectral library of basaltic and secondary minerals, using a linear least squares minimization (Rogers & Aharonson, 2008). A blackbody spectrum was also included in the library to account for differences in spectral contrast between the mixed surface and the library spectra. Modeled abundances were normalized for blackbody abundance to yield areal percentage.

2.3. Geomorphic/Geologic Mapping

Mapping was carried out on a CTX mosaic base map. Unique map units were identified based on remotely sensed surface textures, response to erosion, and relative age as determined by superposition. While

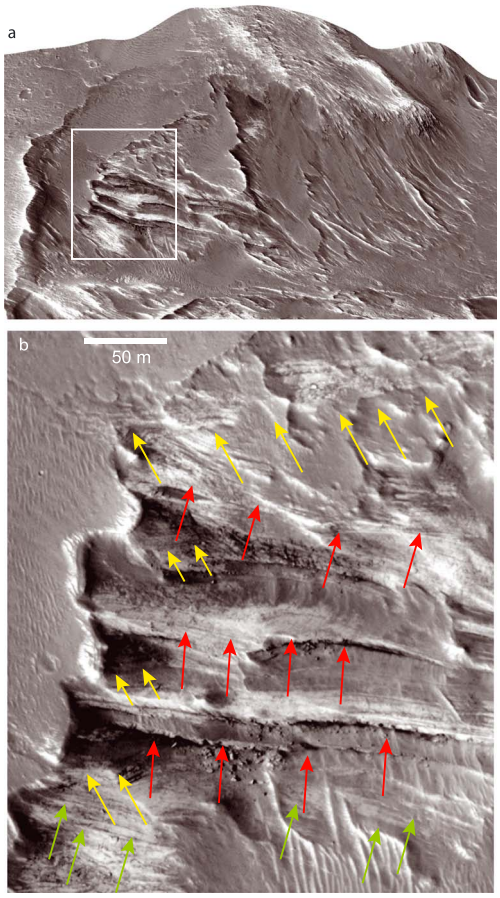

Figure 4. Cliffs at the edge of the platform deposit in the east side of McLaughlin basin show important bedding relationships (looking east). HiRISE image data are draped over CTX DEM data in Figure 4a show multiple bedding orientations in a 3D rendering (3 times vertical exaggeration). A higher-resolution view in 2D shows the flat-lying beds and steeply dipping beds, truncated by flat-lying beds (indicated by arrows of different color), a relationship consistent with deposition in a deltaic environment. These exposures occur hundreds of meters above the modern day basin floor. HiRISE images ESP_028354_2025 and ESP_043070_2025. HiRISE = High-Resolution Imaging Science Experiment; CTX = Context Imager; DEM = digital elevation model.

the mapping was primarily carried out using visible images, the delineation of units was informed by topography, slope map, and thermophysics.

2.4. Crater Counting and Constraints on Surface Ages

Crater counts were carried out using craterstats2 software provided by DLR (Michael & Neukum, 2010), which provide statistical analysis tools as well as an interface to the geographic information system environment (Kneissl et al., 2011). The objective was to estimate minimum surface ages using the distribution of retained craters per unit area (size-frequency distributions) compared against the predicted crater production function of Ivanov (2001). Absolute age estimates were calculated according to the chronology function of Hartmann and Neukum (2001).

3. Results

The results of this work are organized in the following manner. First, we describe the specific observations suggesting that a lake indeed existed in McLaughlin crater. These largely surround the observational clues indicating that a lake surface was present at an elevation 400–500 m above the current basin floor. We then explore the detailed geology of the basin deposits to further test the lake hypothesis and to characterize the environmental conditions and geologic history of that setting.

3.1. Evidence That a Lake Existed in McLaughlin Crater

The rim of McLaughlin crater has eroded, but intact, and has not been breached by any inflowing or outflowing fluvial channels (Figure 2). However, parts of the interior basin wall contain dendritic channel networks of fluvial origin. The most important thing about these channels is that they nearly all terminate at a similar elevation along the eastern crater wall, suggesting that a base level was present when they were active (Figure 2). The average position of the channel termini is −4,635-m MOLA elevation. There are a few channels that have actively eroded below this elevation, but this is not surprising if some of the channels remained active while the lake level decreased or were reactivated later. The average elevation of −4,635 is a minimum value for the high stand of the ancient lake. The deepest part of the McLaughlin basin lies in the west-central part of the basin floor at an elevation of −5,135 m. The suggested base level at −4,635 therefore implies that a lake of minimum depth of ~500 m once existed (Figure 2).

In the same region of the east basin, elevation profiles through the wall show a topographic platform present at an elevation of approximately −4,500 to −4,600 m, just above the putative base level already mentioned (Figure 3). This topography might represent a structurally controlled crater terrace, though it is noted that the landform only occurs in the eastern part of crater basin, where the channels also occur. If the channels reached the lake surface in this area, they would have transitioned from erosion and transport regimes into depositional regimes due to loss of stream velocity, resulting in the formation of a delta. But, the possibility that the topography represents a structural terrace that was modified by erosion cannot be ruled out.

If the platform in the eastern basin does represent a delta, then the eroded, west facing scarp front might show cross-bedded rocks indicative of bottomset, foreset, and topset beds. While much of this scarp has been obscured by younger, draping deposits, some erosional windows do reveal bedding structures in the platform cliff face. HiRISE data draped over CTX-derived DEM data show 3D views of bedding structures in the outcrop (Figure 4). Hundreds of beds as fine as 1-m thick are resolvable in the image. Packages of beds tens of

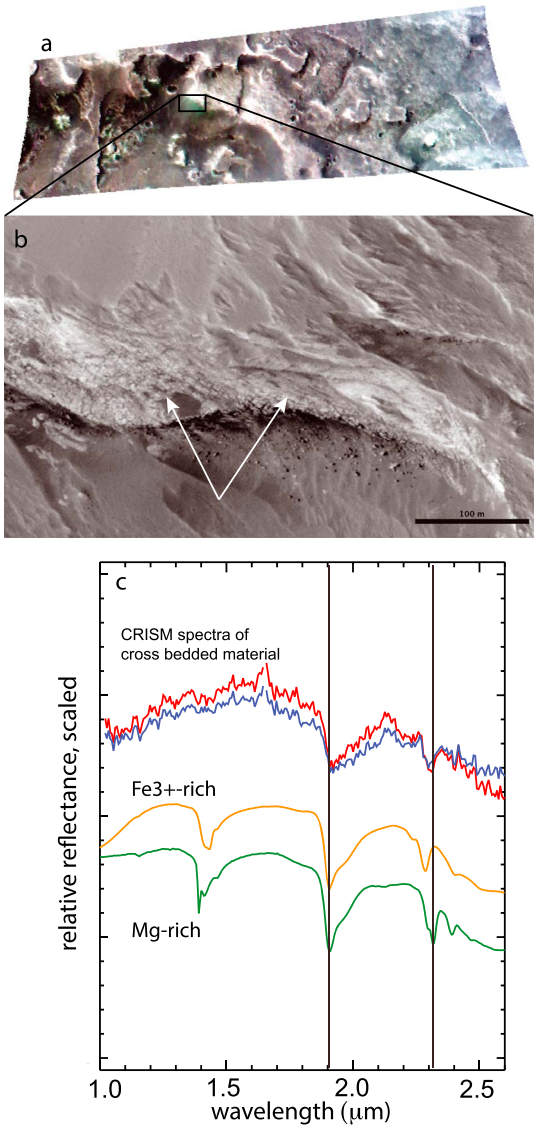

Figure 5. CRISM infrared data of the putative deltaic sediments show evidence for clay minerals. Note that the data were obtained late in the mission after a cryocooler had failed, and therefore, these data are noisier than some others. Even so the data show clear absorptions at 1.9 and 2.3 μm, indicating the presence of Fe-rich, Mg-bearing smectites (e.g., Michalski et al., 2015). CRISM image is FRS2FF3C. CRISM = Compact Reconnaissance Imaging Spectrometer for Mars.

meters thick truncate older beds to produce suites of cross-bedded units consistent with a suite of bottomset, foreset, and topset beds that formed in a delta.

Infrared spectra derived from CRISM data constrain the mineralogy of the cross-bedded materials. The spectra of these deposits contain (Fe, Mg)OH vibrational absorptions suggestive of Fe-rich, Mg-bearing phyllosilicates (Figure 5). The presence of relatively strong HOH vibrational absorptions in the same materials suggests the presence of interlayer water. Taken together, these observations point to the presence of smectite or mixed-layer smectitic clays. The presence of clays within cross-bedded rocks further supports the delta facies model and provides strong evidence that a lake hundreds of meters deep existed in this location.

There is some evidence for shorelines or shore platforms (Irwin & Zimbelman, 2012) present near the putative paleolake level. Throughout the basin, there is a strong break in slope that occurs near the −4,635-m elevation level (Figure 6). Above this level, slopes are generally >10°, and below this level, slopes are <5°. High-resolution imaging across the boundary shows a series of subparallel ridges above, at and below the putative paleolake level. The observations are complicated by the presence of transverse eolian ridges (TARs) throughout the scene. The subparallel ridges might represent strand lines, creep of unconsolidated material toward the basin center (similar to solifluction), eolian landforms, or some combination of these.

Several other regional-scale observations support the idea that the paleolake surface existed near −4,635 m. Thermal inertia data derived from the TES and THEMIS instruments show that the TI values are very different for surface materials located within the basin below the −4,635 elevation compared to similar materials located within the basin (Figure 7), above this level or materials located outside the basin. Materials below the putative base level have TI values ~400–600 and locally as high as 1,000. Similar geological materials located above the base level have TI values of 300 or less. While thermal inertia values are surely affected by the presence of draping deposits and eolian materials as is seen in many crater basins on Mars (Edwards et al., 2009), the clear difference in TI values in and outside the basin (Figure 7) is an indication that something pertaining to basin activity has raised the TI in the basin itself. Such a process could be related to alteration, lithification, and cementation associated with lake waters.

The idea that materials of impact within versus outside the basin origin have different properties is particularly important as related to Keren crater, which deposited ejecta both inside and outside of McLaughlin basin. Keren is a 25-km diameter impact that formed on the southern rim of McLaughlin crater. A crater of Keren's size would theoretically produce an ejecta blanket ~60-m thick at 1 crater radius (12.5 km) from the rim, and of ~7-m thickness at a distance of 3 radii (37.5 km) from the rim (Pike, 1974, Figure 8). Using MOLA elevation data, we delineated the present extent of ejecta from Keren to the south, east, and west (outside McLaughlin), and to the north (inside McLaughlin, Figure 8).

Comparison of the Keren ejecta deposits inside McLaughlin crater to those that were deposited to the south, outside of McLaughlin shows a striking contrast. Despite these units having the same age and same provenance, the morphology of the north versus south ejecta could hardly be more different. Those in the south are comparable to typical Martian ejecta; they contain radial ridges within a hummocky landscape

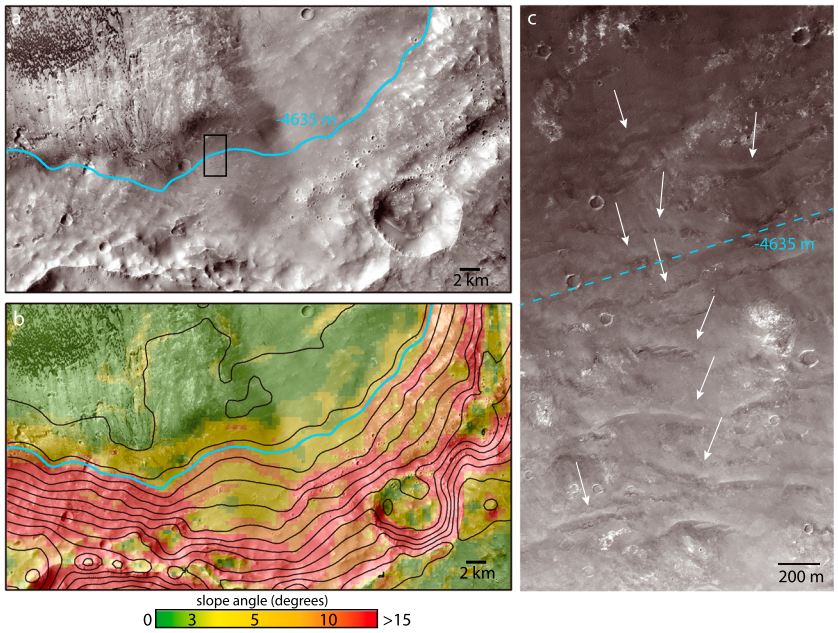

Figure 6. McLaughlin basin contains some evidence for paleo-shorelines. These images are set along the interior of the southern wall of McLaughlin crater. The putative base level of −4,635 m is overlaid on CTX image data (a), MOLA slope data (b), and HiRISE image data (c). Note the change in surface textures above and below this elevation (lower elevations to the north). Slopes below this elevation are <5° and slopes above this elevation are mostly >10°. HiRISE data show some evidence for ridges that could represent terraces or strandlines. But the interpretation of shoreline features is complicated by the presence of subparallel dunes of similar orientation and mass wasting features. HiRISE image ESP_041356_2015. HiRISE = High-Resolution Imaging Science Experiment; CTX = Context Imager; MOLA = Mars Orbiter Laser Altimeter.

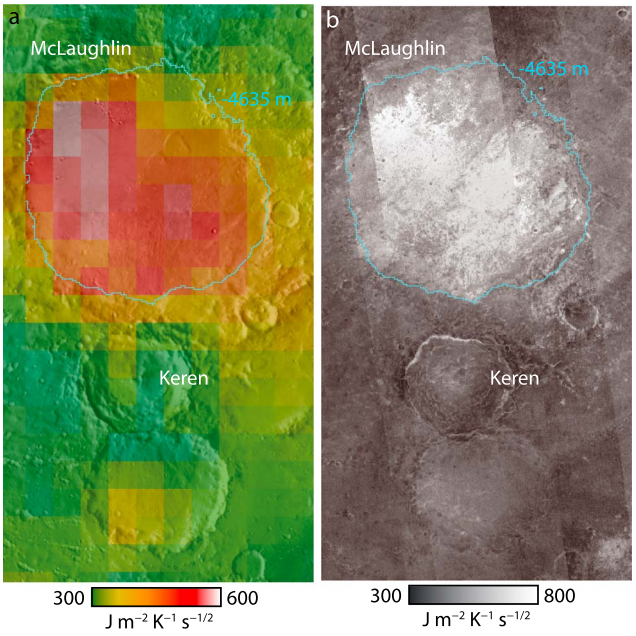

Figure 7. Thermal inertia data measured by TES (left) and THEMIS (right) show strong correlations with the McLaughlin basin. Values are significantly higher (400–600) within McLaughlin basin below the −4,635-m elevation level compared to elevations above this level or surfaces outside the basin (<300). THEMIS = Thermal Emission Imaging System; TES = Thermal Emission Spectrometer.

suggestive of poorly consolidated, fragmented materials that do not form erosionally resistant buttes and hills. By contrast, those to the north are seemingly well lithified, forming steep local topographic ridges, hills, and steep scarps. Yet the north ejecta also exhibit lobate, flow-like patterns (Figure 9). It is possible that the northern ejecta are so different in character from those in the south because the northern ones were either deposited into water or were submerged in water after deposition, whereas the southern parts of the unit have always been exposed subaerially. Furthermore, the crater populations appear different on each surface suggesting that the north one was either protected from cratering for some time or resurfaced; this topic is revisited in the section dedicated to timing below.

Regional-scale spectroscopic imaging using OMEGA data shows additional clues to the geology of Keren's ejecta. A principal component image (PCA)-processed image highlights compositional differences between Keren ejecta deposits beneath the putative base level versus those outside the basin (Figure 10). To evaluate the nature of this difference, we created a spectral ratio of OMEGA I/F data of the Keren deposits located inside McLaughlin divided by those located outside. The result shows spectral differences between the two settings. Despite having the same age and provenance, the Keren deposits inside the McLaughlin basin show absorption at 2.3 μm, which is a key indicator for (Mg, Fe)OH in clays on Mars (Figure 10).

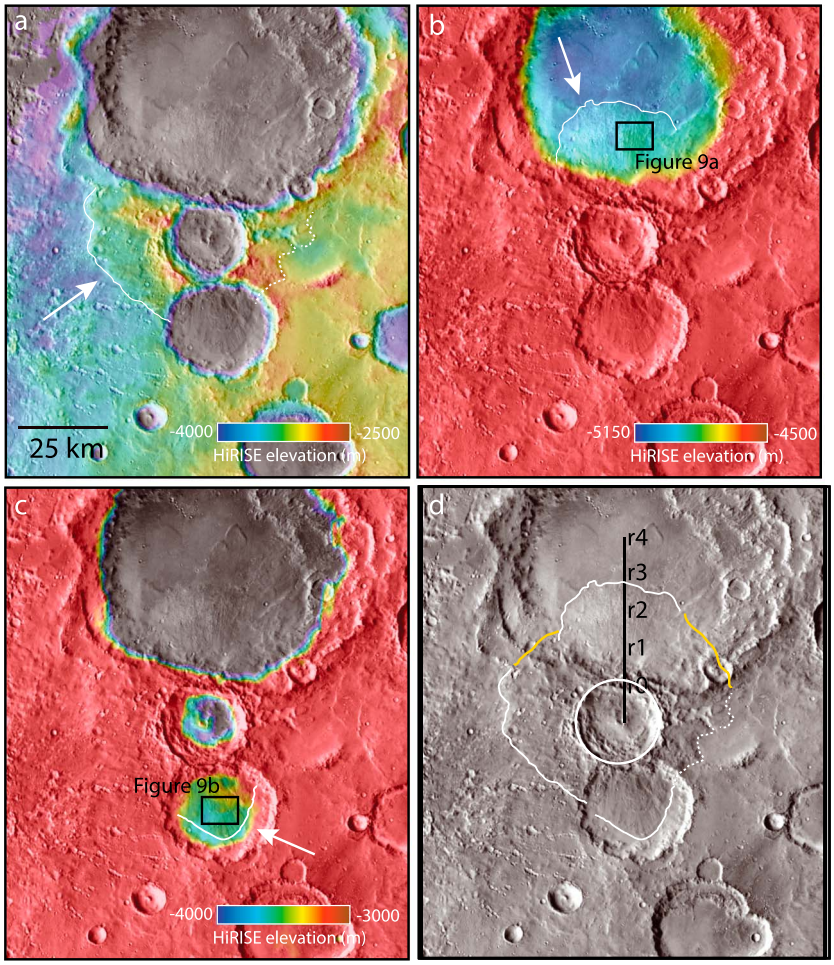

Figure 8. MOLA elevation data draped over THEMIS daytime infrared data were used to identify and delineate Keren's ejecta blanket. MOLA elevation data stretched to different ranges to accentuate the topography of the edge of the ejecta in different areas (a–c). The ejecta are well preserved out to approximately 2 crater radii (from Keren's rim) to the south and west (shown with white line). Ejecta in the east are more eroded. Ejecta to the north, where they were deposited downslope into McLaughlin basin, are preserved out to ~2.5–3 crater radii. (d) The radial distance from Keren crater rim compared to delineated ejecta boundaries. THEMIS = Thermal Emission Imaging System; MOLA = Mars Orbiter Laser Altimeter.

3.2. Geology of the McLaughlin Crater Basin

The McLaughlin crater basin contains vast, complex sedimentary, impact, and hydrothermal deposits, which taken together allow for further testing and refinement of the lacustrine hypothesis. The different deposits are categorized and discussed below according to their geographic setting: south basin deposits, east basin deposits, and central basin (floor) deposits (Figure 11). CRISM spectral indices of images targeted throughout the basin floor show clear evidence for alteration minerals that likely formed in a lacustrine setting (Figure 12). Mineralogy and geology of these deposits are discussed in detail below. In addition, we discuss some unusual lobate materials within the basin floor and dark, draping deposits throughout the basin as two additional categories.

3.2.1. South Basin Units: Deposits Associated With Keren Crater

Ejecta deposits from Keren crater are present throughout the southern portion of the McLaughlin basin. The ejecta might grade into the basin floor deposits, but in the present-day configuration, topographic data and image data suggest a northern margin of this unit (or of the thickest part of this unit) at about three crater radii from the rim of Keren crater (Figure 8). While the ejecta drape much of the southern wall of the basin, there is a clear difference in the morphology and mineralogy of the deposits below the paleolake level (Figures 8–10).

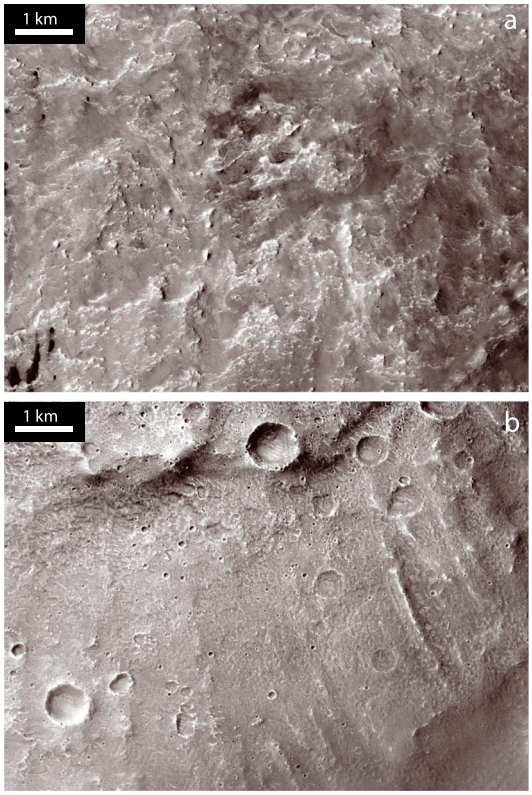

Figure 9. CTX data show the morphology of Keren's ejecta deposits at a distance of nearly 2 crater radii (from Keren's rim) in the north (top) and the south (bottom). There are striking differences between the two deposits. Where the ejecta occur within McLaughlin basin to the north, the deposit displays a rough surface texture with many ridges at the scale of tens to thousands of meters, and the ejecta appear well lithified. In the south, the ejecta are smoother and display a completely different response to erosion, which might reflect differences in lithification/lithology. CTX = Context Imager.

CTX image and DEM data reveal the rough, light-toned, resistant surfaces of the south basin unit, which are partially obscured by dark, draping deposits (Figure 13). High-resolution false color images of erosional windows (Figure 14a) in the ejecta deposits reveal the exceptional diversity of the south basin deposits (Figure 14). Near the northern margin of the deposit (near three crater radii from Keren's rim), the ejecta deposits display clear evidence for complex layering (Figures 14b and 14c). These include strongly blue-green units, infrared-bright units, and red units, as well as bright gray-white units. In some cases, there appear to be only several relatively thick units (Figure 14b) and in other places, hundreds of layers are distinguishable over distances of hundreds of meters (Figure 14c). Some of the layers clearly are discontinuous, pinching out over distances of tens to hundreds of meters. But interactions between surface slope angle and dip angle likely result in complex manifestations of layer exposure. In flatter surfaces, the ejecta deposits display subdued textural patterns rather than clear evidence of layering (Figure 14d).

Some areas display extremely complex mottled color patterns (Figure 14e). It appears that large blocks of disturbed bedrock are present in these types of deposits. These materials contain examples of disturbed layering reminiscent of convolute bedding. Taken together, these complex deposits seemingly correspond to ejecta that have been affected by soft-sediment deformation, as well as debris flow deposits. However, the deposits are lithified as they contain clear evidence for brittle deformation within generally N-S striking faults (Figure 14f).

All of these types of geological surfaces within the south basin deposits display strong, unambiguous evidence for pervasive and intense aqueous alteration in CRISM infrared data (Figure 15). As noted previously by Ehlmann et al. (2010), this site is one of the strongest signals of serpentinization on Mars. The strongest spectral signatures of serpentine correspond to fractured bedrock containing light-toned veins approximately 1 m across (Figures 15b and 15c). The composition of the veins is not discernible with current data because, though prominent and easily resolved in the 0.25-cm/pixel visible images, they compose only a very small spatial fraction of the area of 18-m/pixel infrared data. As discussed in more detail further below, Mg-rich carbonate contains some similar features to Mg-rich serpentine minerals. If magnesite occurred with serpentine as veins, it would be difficult to positively identify (Brown et al., 2010). The synthesis section contains more treatment of this issue.

While the strongest spectral signatures of serpentine/carbonate correspond roughly to rocky and vein-bearing surfaces, it is important to note that some of the convoluted, layered, and mottled ejecta materials contain similar spectral features of comparable strength. Most of layered or disrupted parts of the unit display clear evidence for metal-OH absorptions at 2.3–2.305 μm indicative of FeOH and slightly steeper spectral slope from 1 to 2 μm consistent with higher Fe content. These features along with the fact that the water absorption at 1.92 μm is narrower in the layered or disrupted unit suggest at least one additional phyllosilicate is present, likely a Mg-bearing and Fe-rich smectite (Michalski et al., 2015).

3.2.2. East Basin Deposits

A high-resolution DEM of the central and eastern parts of the basin reveals a range of deposits present at elevations below the putative paleolake surface of −4,635 m (Figure 16). In the eastern part of McLaughlin basin is a broad wedge of material that slopes upward from the basin floor at an elevation of −5,100 m eastward to an elevation of approximately −4,900 m. Most of the unit consists of rough, light-toned bedrock (Figure 16c) that has eroded into irregular ridges (Figures 16c and 16d). Many of these ridges likely represent retreating scarps along bedding planes though others appear in swarms

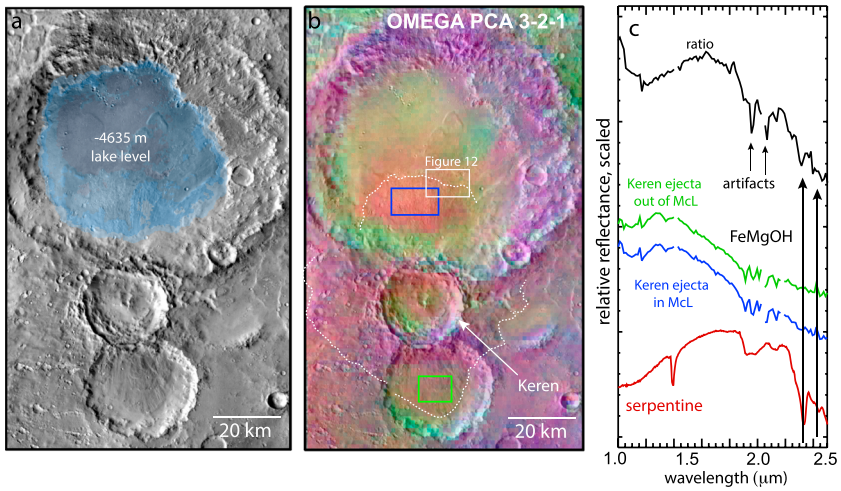

Figure 10. (a) THEMIS daytime infrared data of McLaughlin crater. MOLA data are overlaid, where elevations above the −4,635-m proposed base level are omitted and data below the base level are colorized in blue colors. (b) OMEGA near-infrared data processed into principal components where PC3 is red, PC2 is green, and PC1 is blue. Note that PCA data bring out spectroscopic differences as qualitative differences in color, but the colors have no direct meaning. The PCA image shows that Keren's ejecta have a different spectral character where they occur in McLaughlin crater, below the putative base level compared to where they occur outside the basin. OMEGA I/F spectra were averaged from regions of interest inside (blue) and outside the basin (green). Ratio of the average spectrum inside the basin divided by the average spectrum from outside the basin illustrates that the ejecta inside the basin contain absorptions at ~ 2.3 μm attributable to the presence of phyllosilicates within the Keren ejecta inside McLaughlin basin. The white box in Figure 10b marks the context of Figure 12. THEMIS = Thermal Emission Imaging System; MOLA = Mars Orbiter Laser Altimeter; OMEGA = Observatoire pour la Minéralogie, l'Eau, les Glaces et l'Activité; PCA = principal component image.

suggesting of mineralized fractures now exposed in relief. Subhorizontal bedding is clearly revealed in some areas, though overall the topographic relief in the unit is subdued compared to that of the south basin deposits.

CRISM infrared data of the light-toned bedrock show that Fe-rich clays are present throughout the east basin deposits (Figure 17). While the CRISM data available in this part of the basin are slightly noisy because all are FRS images collected after failure of one of the cryocoolers, the data unambiguously show a narrow HOH feature at 1.92 and an FeOH vibration at 2.3 μm. The spectral shape of these materials stands in contrast to that observed in most of the south basin deposits, where serpentine is common.

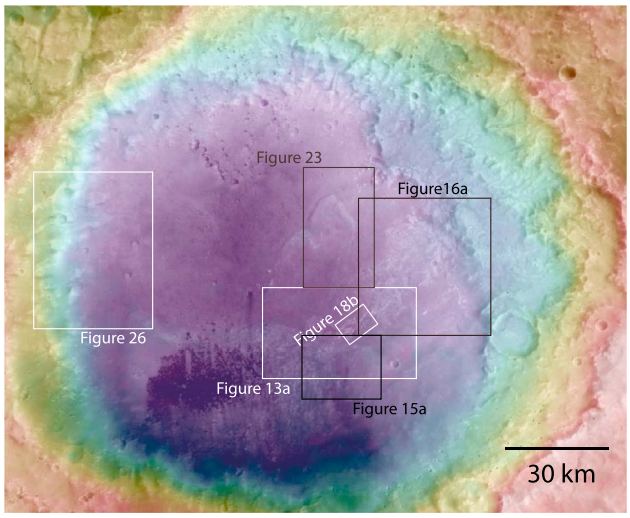

Figure 11. HRSC data illustrate the context of key figures discussed in detail elsewhere in the paper. HRSC = High-Resolution Stereo Camera.

3.2.3. Central Basin Floor Deposits

Based on comparison to other ancient, flat-floored craters (Edwards et al., 2014), it is likely that the basin floor contains deposits that are thousands of meters thick. In general, these materials are poorly exposed nearly everywhere they occur, with one important exception. A NE-SW trending canyon containing cliffs 70-m high reveals the complex 3D geology of the deep basin deposits (Figure 18).

Layering within the deep basin unit is best exposed in the northern wall (south facing wall) of the canyon, which rises ~50–70 m above the canyon floor. In some areas, layers or packages of layers ~5-m thick are nearly horizontal and continuous over >500 m laterally (Figure 19). In other areas, bedding is more convoluted, occurring in thicker (~20 m) beds that in some places appear massive, but generally shows systems of antiformal-synformal structural relationships within the bedding plane (Figure 20). Some observations of the *convolute bedding* are indistinguishable from what might be cross-sectional views of channels. Elsewhere, ~10-m thick beds display large-scale angular bedding (Figure 19). Similar units are

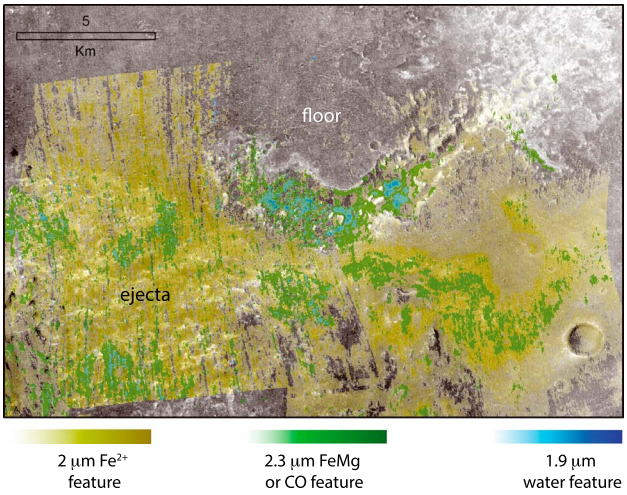

Figure 12. A mosaic of CRISM band parameter maps was overlaid on HRSC image data to provide an introduction to the mineralogy of the McLaughlin basin. The 2-μm feature corresponds to electronic transitions, mostly in pyroxenes. The 2.3-μm feature measures Fe,Mg-OH vibrational overtones in phyllosilicates (smectite clays, as well as serpentine-group minerals). This feature also detects the C-O absorption in carbonate minerals, which is shifted to ~2.3 μm when the carbonate is Mg rich. The 1.9-μm feature corresponds to HOH vibrations in hydrated minerals, including both clay minerals and hydrated carbonates. Note that the floor of the canyon is draped by a dark, pyroxene-bearing material. Windows through this draping unit show strong 1.9- and 2.3-μm absorptions in the ejecta and basin floor materials. CRISM images are FRS2C9DC, FRS35729, FRS3705A, FRTA27C, and FRTA5AA. HRSC = High-Resolution Stereo Camera; CRISM = Compact Reconnaissance Imaging Spectrometer for Mars.

observed throughout the northern wall of the canyon, though the exposures are obscured by slope failure in some places.

HiRISE false color data draped onto a HiRISE DEM show 3D color patterns that are potentially related to composition, grain size, and/or depositional environment (Figure 21). The planar-bedded materials appear to form packages of three units: (1) a thick sequence of cliff-forming material, (2) a thin bed of very light-toned material, and (3) a thin bed of dark-toned material. This package of three units might represent cyclic depositional environments, perhaps involving periods of more energetic versus more quiescent deposition or periods dominated by detrital versus authigenic deposition.

CRISM infrared observations of the deep basin unit exposed in the canyon contain strong absorptions of alteration minerals (Figure 22). The deep basin materials contain spectral absorptions at 1.4, 1.91, 2.3, 2.39, and 2.52 μm. This suite of features is most consistent with the presence of Fe-rich dioctahedral smectite with a high Mg content (i.e., Mg-rich nontronite). However, the deep absorption from 2.3 to >2.5 μm strongly suggests the presence of admixed minerals that also contain features in this wavelength range such as carbonate minerals. The possibility that carbonate is also present is discussed in detail in the discussion section below.

3.2.4. Lobate Materials

One of the most fascinating aspects of the geology of McLaughlin basin is the presence of lobate deposits on the crater floor. These deposits occur as two sets of overlapping concave-south arcuate ridges that rise approximately 20 m above the abyssal plains. Though the exposures are poor, HiRISE data show a series of ridges in the lobes that suggest the presence of horizontal layering (Figure 23). There are several possible origins for the lobate materials including impact ejecta and subaqueous density flow (or turbidite) deposits. In fact, these origins might be fundamentally linked, as described below.

CRISM spectra of the deposits show evidence for Fe-rich clays as observed in other parts of the basin. The only available data are FRS images that postdate failure of the cryocoolers, and therefore, the data are unfortunately noisy. Despite this challenge, it is clear that the deposits contain absorptions at 2.3 μm indicative of Mg-bearing, Fe-rich clay minerals (Figure 24). Whichever process resulted in formation of the lobate materials, it involved alteration or mobilization of clay-rich materials.

Figure 25 shows two sets of flow deposits in the south and central part of the basin. The more southern deposits (marked with black arrows in Figure 25) occur in the place where ejecta from Keren crater are likely to occur, approximately 2–3 crater radii from the rim of Keren. The second set of flows (marked by yellow arrows in Figure 25) appears to have a similar flow direction but occurs approximately 4–5 crater radii from Keren. The further set of lobate deposits is unlikely to represent subaerial ejecta from Keren based on mineralogy, thickness, and distance from Keren Crater.

The abyssal lobate deposits appear to have been deposited as flows from the south toward the north and are potentially genetically linked to slope instability on the south wall of McLaughlin crater (Figure 25). The south basin deposits contain clear evidence for landslides that are 100- to 150-m thick (marked by red arrows in Figure 25). Age relationships between the landslides present in the south basin and the abyssal deposits are difficult to determine with certainty. It is possible that the same event that created the thick landslide deposits in the south basin resulted in density flows along the basin floor. In fact, if the landslides occurred when water and fine-grained sediment were in the basin, turbidites would be an inescapable consequence.

On Earth, our understanding of turbidite geology is defined largely by stratigraphy of ancient turbidite deposits and seismic imaging of the modern seafloor. On the modern seafloor, 3D seismic imagine shows slump deposits at basin margins and subaqueous channels that ultimately become filled and buried with

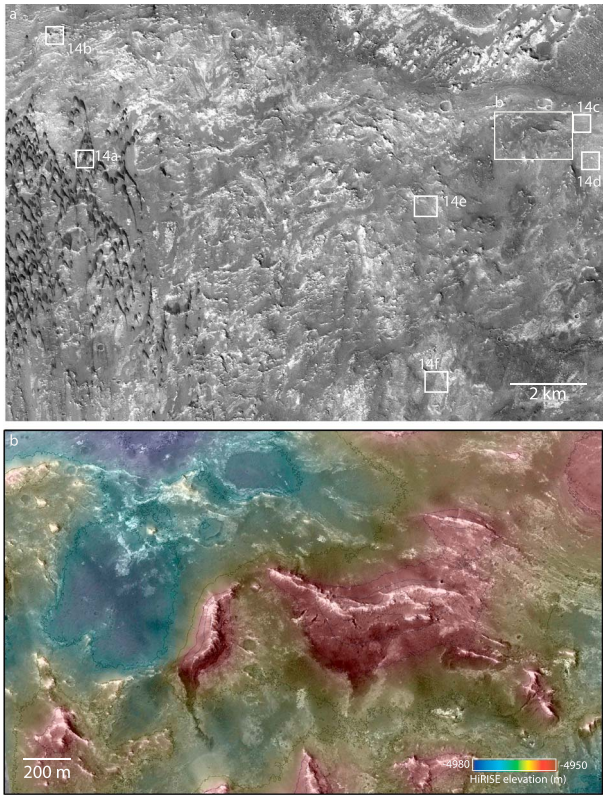

Figure 13. A CTX image shows the morphology of the south basin deposits and provides context for high-resolution views from HiRISE shown in Figure 14. Note the exposure of light- and dark-toned, lobate, layered deposits that occur in sloping surfaces as well as resistant ridges (a). A HiRISE DEM shows the relief of resistant ridges, which reach up to 30 m above the surrounding terrain (b). HiRISE image DTEEC_007599_2020_007454_2020_U01. HiRISE = High-Resolution Imaging Science Experiment; CTX = Context Imager; DEM = digital elevation model.

sediment (Posamentier & Kolla, 2003). As material is transported further into the basin, the system transitions into a distributary system, which on flat-floored basins result in paddle-shaped frontal splay deposits (as seen in map view) that are tens of meters thick and tens of kilometers long (Posamentier & Kolla, 2003). This geometry is precisely what is observed in McLaughlin crater, and while morphological similarity is not a proof of similar origins, it does provide a compelling case for turbidite flow in the floor of McLaughlin basin.

The stratigraphy of the putative turbidite deposits is exposed in the canyon wall in the floor of McLaughlin crater (Figures 18–20). Figure 20 illustrates convolute bedding and cross bedding in the central and west parts of the canyon wall that likely represent the interior of these flows. Concave up bedforms and subhorizontal layers (Figures 19 and 20) are potentially evidence for buried channel deposits and stacked sand sheets (Posamentier & Kolla, 2003). The complex bedding relationships combined with mineralogical and contextual evidence for deposition in deep water all add up to the conclusion that these lobate deposits likely represent turbidites, as this combination of observations and contextual setting is unlikely to be explained by subaerial deposition of ejecta or subaerial landslides alone.

Lobate deposits present in the central and south parts of the basin are unique in their exposure but might not be unique deposits. In fact, the west basin also contains broad, low-relief flow deposits originating in the west wall (Figure 26). Though the runout distance is lower and the length/thickness ratio is lower for the west basin lobate deposits, these likely also represent subaqueous density flows based on their context and geometry.

All of these observations being noted, the fact remains that the morphology of the northern ejecta of Keren is superficially similar to fluidized ejecta observed in rampart craters, and therefore, a mechanism that produced or preserved fluidized ejecta toward the north (topography?) and not the south might explain the deposits. The mechanisms that produce rampart craters are thought to involve ice-rich terrain in some cases but in other cases are not well constrained. We acknowledge that there are unknown elements to the geology of Keren's ejecta, but we do not see evidence for ice-rich terrains. Our preferred hypothesis is that the occurrence of abundant hydrated minerals, the long run-out distances, the unusual convolute bedding, and the spatial and temporal contexts within the McLaughlin crater basin all point to deposition in a lake. However, the most important point is that the excellent cross sectional exposures of Keren ejecta within Mclaughlin crater would provide unprecedented opportunity to study Martian ejecta in situ.

3.2.5. Dark Mantling Materials

A dark-toned unit occurs throughout the floor of McLaughlin crater. HiRISE images show a brownish hued unit of variable thickness (up to ~10 m) that mantles underlying topography (Figure 27). In some parts of the basin, this unit is extremely thin or absent (especially the south and east basin areas). In other parts of the basin, it is thick enough to obscure underlying geology. CRISM data show that the unit is largely spectrally unremarkable but does contain weak, broad Fe^{2+} features consistent with the presence of pyroxene or mafic glass (Horgan et al., 2014). While the capping unit occurs in patches at a range of elevations, it is most evident where it mantles the abyssal basin floor. In that stable, low-slope context, it has accumulated and preserved a large number of small craters, a feature characteristic of this unit.

It is likely that the *dark materials* lumped into one unit here actually represent multiple geological units. There are certainly some unconsolidated dark sandy deposits, but there is strong evidence for older

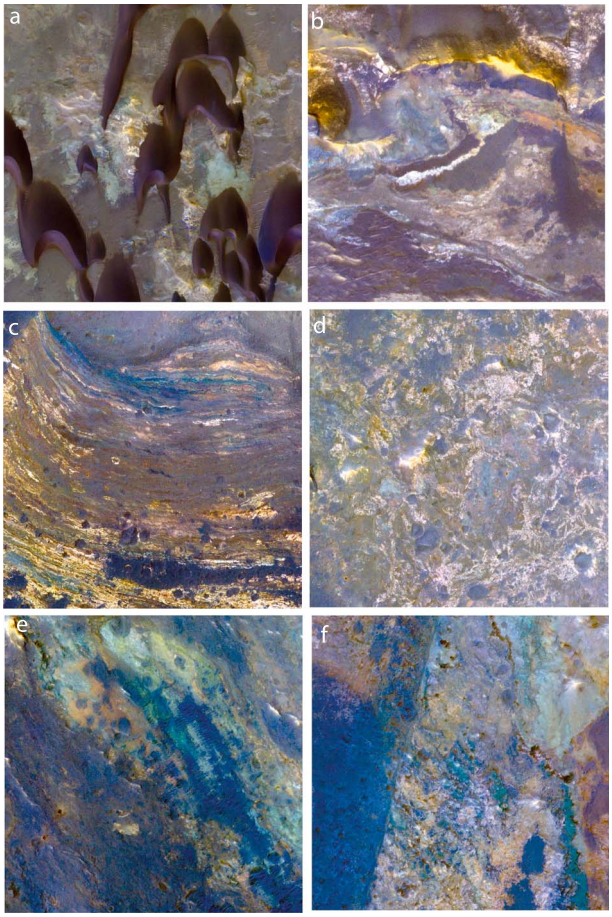

Figure 14. High-resolution false color images from HiRISE show important characteristics of the south basin deposits (a–f). All HiRISE images are IRB (infrared, red and blue-green channels assigned to RGB in the false color images shown), and images are approximately 500 m across. Colorful, tilted, layered deposits are observed in windows where the substrate is not masked by overlying dark, draping deposits or modern dunes (a). The color boundaries can be sharp and complex (b), suggesting structurally complicated lithologic boundaries or complex structural controls on alteration. In some places, >50 layer boundaries are easily discernible over short distances (c), though it is not clear that each layer is laterally continuous. In other areas, the lithologic boundaries appear diffuse or gradual (d). Some parts of the deposit show similar false color units, but the surface is strongly mottled and physically disrupted (e), consistent with bedrock blocks within a debris flow. The south basin units contain faults juxtaposing units of distinct morphologic and color character (f). HiRISE images include PSP_007454_2020_COLOR, ESP_042991_2020_COLOR, and ESP_026666_2020_COLOR. HiRISE = High-Resolution Imaging Science Experiment.

generations of consolidated dark cover as well. In some rare cases, the dark mantling materials have strong spectral character. Some patches of TARs (Balme et al., 2008) overlying the south basin deposits are strikingly olivine rich in CRISM data. These could represent a more ancient generation of sand dunes with distal sources of olivine no longer available. More likely, the olivine-rich TARs present only in the south basin deposits represent a local source of olivine grains of appropriate grain size sourced from local bedrock.

3.2.6. Geology of the Basin: Detailed Mineralogy

With the exception of the dark-toned, draping deposits, essentially all of the deposits within McLaughlin crater basin, contain evidence for Fe and Mg-rich phyllosilicates—to the extent that CRISM data are available. The strongest spectral absorptions are found in the central basin floor deposits, which appear spectrally dominated by Fe-rich smectitic clays, and the south basin deposits (Keren ejecta), which appear dominated by serpentine-group minerals, carbonates, or both. Below, we address these two key questions: (1) are the spectra of the south basin features indicative of carbonate or serpentine? And (2) what is the bulk composition of these altered units? In other words, are the phyllosilicates or carbonates abundant phases?

3.2.6.1. Do the South Basin Deposits Contain Serpentine or Carbonates?

The strongest spectral absorptions of serpentines in the wavelength range accessible by CRISM correspond to OH overtones present at ~1.39 μm, overtones of adsorbed HOH at 1.91 μm, absorptions at 2.12 μm, and MgOH combination bands at 2.31–2.33 and 2.50–2.52 μm. Even modest amounts of substitution of Fe^{2+} for Mg^{2+} in serpentine minerals result in strong electronic absorptions in the 1- to 2-μm range, resulting in a strong spectral slope in this region. This suite of spectral features allows for confident detection of serpentines on Mars from CRISM data and indeed a global survey noted their occurrence in McLaughlin crater (Ehlmann et al., 2010), though these detections have since received little mention.

A complicating issue in detection of serpentine using infrared reflectance spectroscopy is that the two strongest absorptions related to MgOH overlap with the two strongest absorptions in some carbonate minerals, especially Mg-rich carbonates (Ehlmann, Mustard, Murchie, et al., 2008). The most diagnostic features of carbonates in the CRISM spectral range correspond to (Ca, Fe, Mg)CO_3 vibration overtones located in the 2.29 to 2.34-μm range and 2.48- to 2.53-μm range. Because Mg^{2+}, Ca^{2+}, and Fe^{2+} cations have different sizes and produce different bond lengths and energies, this pair of cation-CO_3 absorptions shifts from lower wavelength in the case of Mg-rich carbonates to larger wavelength in the case Ca and Fe carbonates. Unfortunately, the MgOH overtones in some serpentines overlap with $MgCO_3$ overtones in some carbonates. To make matters more complicated, carbonates and serpentines commonly occur together in nature. However, in detail the two are distinguishable because (a) the spectral shapes of carbonates and serpentines are overall different enough to be addressed with spectral modeling over a larger spectral range and (b) carbonates contain another set of CO_3 overtones at longer wavelengths (3.4 and 3.9 μm) that are completely absent in serpentines.

While broadly similar, the differences in spectral detail between serpentine and carbonate allow for their distinction. Figure 28 shows a portion of the floor of McLaughlin crater containing both central basin floor deposits in the canyon and south basin deposits. The figure includes CRISM spectral indices

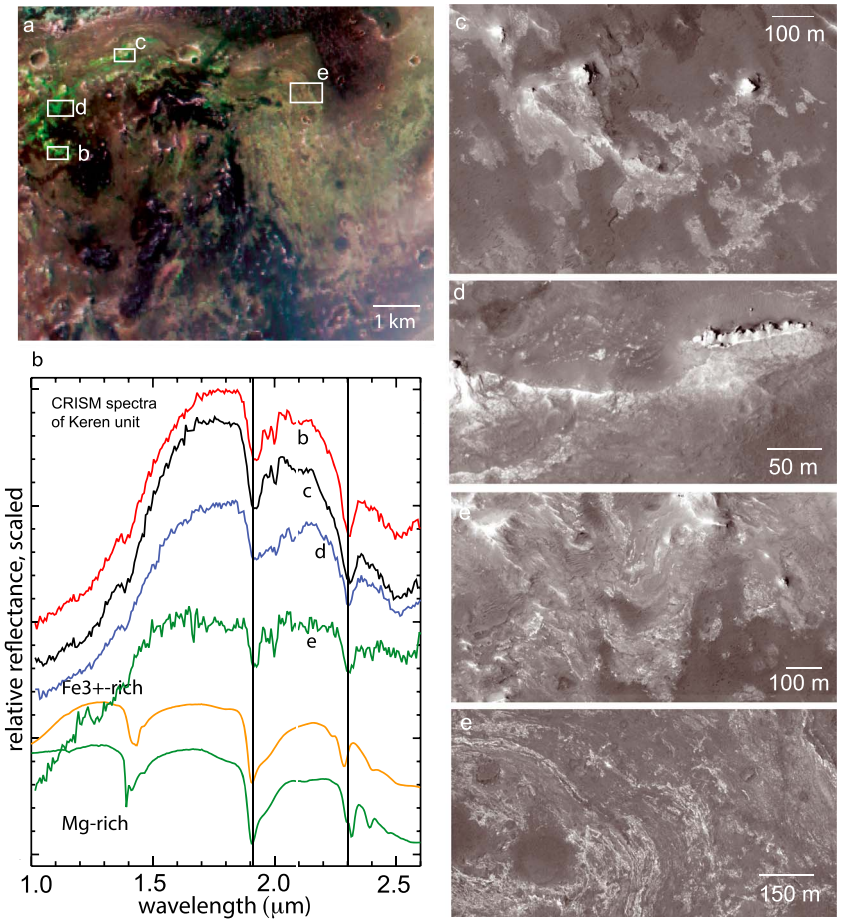

Figure 15. CRISM infrared data of the south basin deposits show evidence for serpentinization. A subset of a CRISM FRT image (R, 2.38 μm; G, 1.80 μm; and B, 1.15 μm) shows the locations from where spectra were extracted. Altered surfaces appear green in this false color image. Extracted spectra show clear evidence for absorptions at approximately 1.4, 1.9, 2.1, 2.3, and 2.5 μm consistent with the occurrence of serpentine group minerals and Mg-rich, hydrated carbonates (b). HiRISE views of the precise surfaces where the serpentine-like spectra were measured show intact, tilted bedrock (c), tilted rock cut by ~1-m-thick bright veins (d), and convoluted or folded bedrock reminiscent of soft-sediment deformation (e). The area of debris-flow like surfaces described in Figure 14c is shown here in Figure 15f. This surface contains similar spectral features as the others described in this figure, but the features are not as prominent and display more noise. CRISM image is FRTA5AA. HiRISE = High-Resolution Imaging Science Experiment; CRISM = Compact Reconnaissance Imaging Spectrometer for Mars; FRT = full resolution targeted.

designed to accentuate specific spectral features related to serpentine and carbonates (Viviano-Beck et al., 2014). The BD2300 (where BD2300 corresponds to band depth at 2,300 nm) detects (Fe,Mg)OH features in serpentine, smectitic clays, and other ferromagnesian phyllosilicates. The BD2295 + BD2500 index is formulated to distinguish Mg carbonates, which should contain both of these features together. A BD3400 index is aimed to identify longer wavelength CO_3 overtones unique to carbonates.

Figure 28 shows that the scene contains widespread Fe and Mg-rich phyllosilicates, but the two indices designed to distinguish carbonates show only localized occurrences of those phases.

Spectra extracted from the floor of the canyon are compared to spectra of mineralized blocks within the south basin deposits in Figure 28e. Note that the south basin deposits contain features discernible at ~3.4 μm indicative of the presence of carbonates—though this feature is weak—suggesting that carbonates might not be abundant. Further interpretation requires spectral modeling.

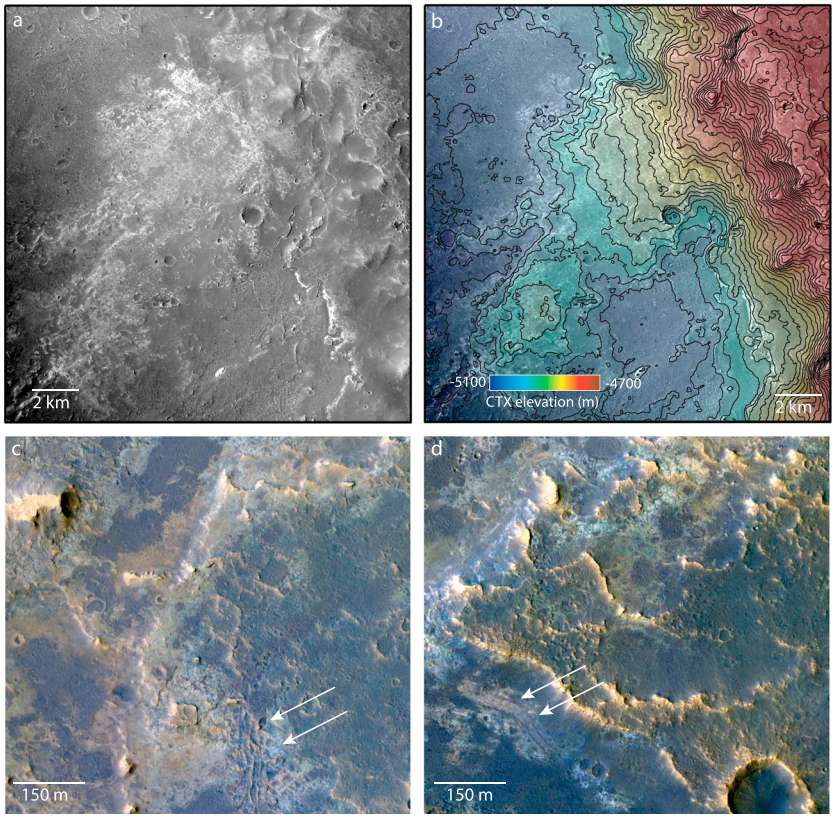

Figure 16. (a) A CTX image shows light-toned deposits on the east side of the McLaughlin basin floor (east basin deposits). (b) This deposit includes a shallowly dipping stack of sediments exposed over an elevation range >150 m (10-m contours are shown). These deposits are located southwest of the putative delta deposits located within a topographic platform in the eastern side of the basin. (c) The deposit contains exposures of colorful, light-toned deposits in low-relief, flat exposures as well as within a series of irregular ridges that might represent recessive erosion of bedding planes. Eroded surfaces in some places show networks of irregular ridges more resistant to erosion (white arrows), which potentially represent fracture zones mineralized by diagenetic fluids. Some scarps reveal layers with outcrop traces that seem to follow topography (d), suggesting shallow dips in some units truncating steeper dipping units lower in section (white arrows). HiRISE stamps include ESP_044191_2020_RED and ESP_035237_2020_RED. CTX = Context Imager; HiRISE = High-Resolution Imaging Science Experiment.

3.2.6.2. What Are the Abundances of Alteration Minerals and Primary Minerals in the McLaughlin Basin Units?

The CRISM scene covering the deposits of interest was atmospherically corrected using the DISORT radiative transfer model, resulting in surface single-scattering albedo values, which can then be modeled using a combination of guided inputs for candidate library spectra and ranges of anticipated grain sizes (Figure 29). This same process applied to each pixel in a CRISM image provides abundance maps (Table 1), which allow for interpretation of the mineralogy of different geological units (Figure 30).

Spectral modeling results are consistent with interpretations of spectral index maps, though the abundance maps produce stronger constraints on the mineralogy and are scaled to show stricter constraints on the mineral distribution. Both the central basin floor deposits and the south basin (Keren ejecta) deposits are dominated by the following mineral groups: (a) pyroxene, (b) olivine, (c) serpentine, and (d) smectite. The central basin floor deposits also contain significant abundances of ferrihydrite, which is not modeled at all in the south basin deposits. Note that, in addition to the major phases modeled in *high* abundances (tens of percent), the models also result in a number of phases modeled in small abundances with values near the error level of the technique.

The spectral models shed some light on the carbonate-serpentine problem. Using a full, unrestricted library of reference spectra, the technique results in only minor abundances of modeled carbonates (~3%) and large

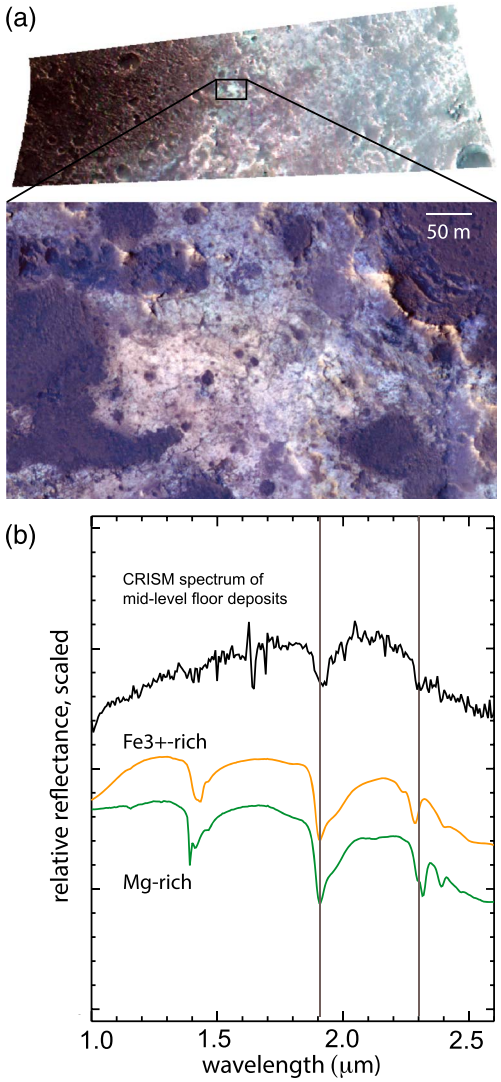

Figure 17. CRISM infrared spectra of east basin deposits show the presence of Fe,Mg-rich clay minerals. Light-toned deposits with blue-green hues in the CRISM false color image (R, 2.38 μm; G, 1.80 μm; and B, 1.15 μm) correspond to clay-bearing surfaces (a). HiRISE IRB data show the surface from which CRISM data were extracted (b). The CRISM ratio spectrum shows a strong absorption at 1.9 μm and a weaker but detectable feature at 2.3 μm. These suggest the presence of Fe,Mg clay minerals. Note that the CRISM image was obtained after the failure of a cryocooler, resulting in noisier data. CRISM image is FRS35729. HiRISE = High-Resolution Imaging Science Experiment; CRISM = Compact Reconnaissance Imaging Spectrometer for Mars.

amounts of modeled serpentine (~35%), suggesting that minor carbonates could exist, but the overall spectral shape is better fit by serpentine group minerals. A way to test this result further is to limit the spectral reference library fed into the model. This is done by running the models through steps in which certain mineral groups were omitted. In other words, we have run the models with serpentine minerals omitted to see if the algorithm shows substantially higher carbonates. This technique has been carried successfully before (Ruff et al., 2006) to demonstrate which mineral groups are essential to model the observed spectra. In this case, omitting serpentine results in only modest increases in modeled carbonate abundances (~7%).

Based on the combination of spectral index mapping (Figures 28a–28d), comparison of extracted spectra (Figure 28e), and spectral model results (Figure 30), it very likely that serpentine is present in substantial proportions in the deposits—especially the south basin (Keren ejecta) deposits. Carbonate minerals are very likely also present, as evidenced by the spectral index maps, long wavelength spectra features (near 3.4 μm), and the modeled abundances. However, carbonates are likely only a minor phase by volume. Such an interpretation is consistent with the surface texture and brightness relationships in the serpentinized rocks in HiRISE data (Figures 15b and 15c). High-resolution images show these units to be composed of resistant, medium-toned bedrock that is cut by ~1 m-thick, bright, resistant veins. The relative surface area of these two materials is consistent with serpentine bedrock cut by bright carbonate veins that compose <5% of the bedrock by volume.

Other key points from the spectral modeling results include the following. First, the layered canyon floor deposits are rich in smectite and contain lesser abundances of serpentine, while phyllosilicates in the south basin deposits are dominated by serpentine with little smectite. Second, the central basin floor deposits contain significant abundances (~16%) of ferrihydrite while the south basin deposits show no evidence for this material. Third, despite the intense amount of alteration present in both units, they both contain significant abundances of primary minerals (pyroxene and olivine, totalling 40–50%). In the central basin floor deposits, this material might represent detrital sediment. Though modern, dark sand might contribute to these modeled abundances, dark patches of sand are unlikely to explain these significant abundances of primary minerals because high-resolution images show relatively bright, well exposed surfaces. Some of these surfaces have high slopes where sand is not likely to accumulate. In the south basin deposits, modeled primary minerals might also include detrital inputs. But in this context, the igneous phases might also represent crustal materials exhumed by the Keren impact or the McLaughlin wall rock that has been deposited through mass wasting. The primary phases might indicate incomplete alteration of the protolith. However, in the south basin, untangling the influence of dark mantling materials is more challenging because many surfaces contain irregular patches of dark sand.

Mineral abundances obtained by CRISM spectral modeling can be tested against results obtained by spectral modeling of TES data, though the TES data measure an area thousands of times larger than CRISM. TES emissivity spectra averaged from a ~9 × 27-km area located within the south basin deposits produce comparable mineral abundances to those of CRISM data for outcrops in the same unit (Figure 31). The only major difference between the TES and CRISM results is that the TES models indicate ~30% plagioclase while the CRISM models do not indicate plagioclase. This result is not entirely surprising because feldspars are featureless in the CRISM spectral range, unless they contain Fe^{2+} (which is uncommon).

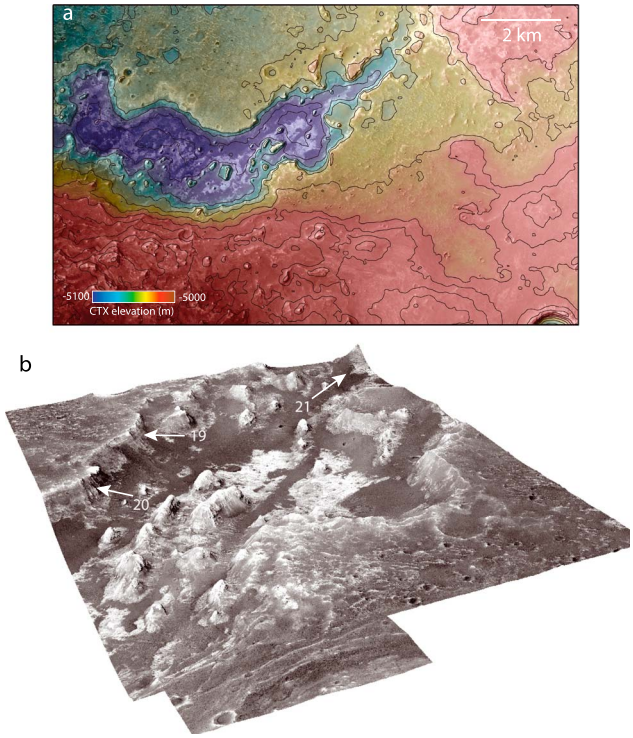

Figure 18. A NE-SW trending canyon in the south-central portion of McLaughlin basin exposes the central basin deposits. CTX DEM data draped over CTX image data (a) show the relationship among the south basin, east basin, and central basin deposits, which are flatter lying and occur at lower elevation. A HiRISE image draped over HiRISE DEM data shows the canyon in 3D (looking toward the northeast). South facing cliffs ~100-m high in the north rim of the canyon reveal important bedding relationships in these basin floor deposits, shown in detail in Figures 19–21. HiRISE = High-Resolution Imaging Science Experiment; CTX = Context Imager; DEM = digital elevation model.

While their contribution as a *graybody* can be modeled accurately in some cases, lack of modeled abundances in the near infrared is not an indication of absence in the case of feldspar. When TES modeled mineral abundances are normalized to zero feldspar for comparison with CRISM, the modeled mineral abundances are nearly identical (Figure 31).

3.2.7. Geology of the Basin: Geomorphic/Geologic Mapping

A geologic map was constructed based on the geomorphology and mineralogy of units observed throughout McLaughlin crater. The objective of the mapping was to capture the geologic history of the basin, and as such, the units were delineated based on their observable geomorphic, sedimentological, stratigraphic, and mineralogical properties, as well as geographic setting within the basin (Figure 32). Thirteen geologic units are described below, grouped, and ordered based on observed contact relationships and relative age, from oldest to youngest.

Noachian plains deposits (npl) are undifferentiated in this work. They represent ancient crust that was impacted by the bolide that produced McLaughlin impact crater. The Noachian plains include fractured and eroded volcanic, sedimentary, and impact-generated materials.

McLaughlin crater *wall rock and rim materials* (mwr) include fractured materials produced by the impact event that created McLaughlin crater. Most of the ejecta from the impact are lost to erosion or are otherwise not distinguishable from unit npl. The rim and wall rock include significant mass wasting deposits. In the eastern part of the basin, the wall has been eroded by fluvial channels.

Central basin sedimentary deposits (cbs) are the oldest observable sedimentary deposits in the basin. The NE-SW oriented canyon eroded into the crater floor exposes layered deposits to a depth of ~100 m below the modern crater floor. To the greatest depth observable, these units contain interbedded light- and dark-toned clay- and ferrihydrite-rich layers. The uppermost beds of this unit appear gradational or interbedded with

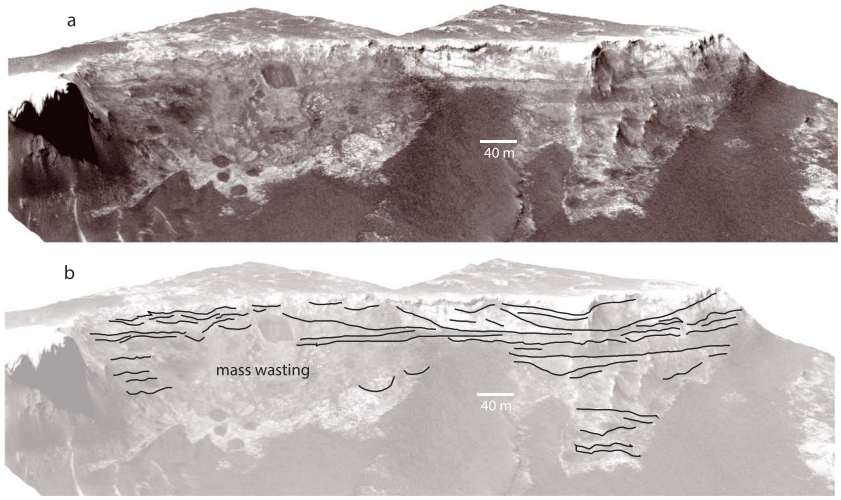

Figure 19. Three-dimensional renderings of HiRISE data of the cliffs in the canyon reveal complex primary structures within the basin floor deposits. Planar and trough cross bedding is observed among beds ~10-m thick (a). HiRISE image is DTEEC_007599_2020_007454_2020_U01. HiRISE = High-Resolution Imaging Science Experiment.

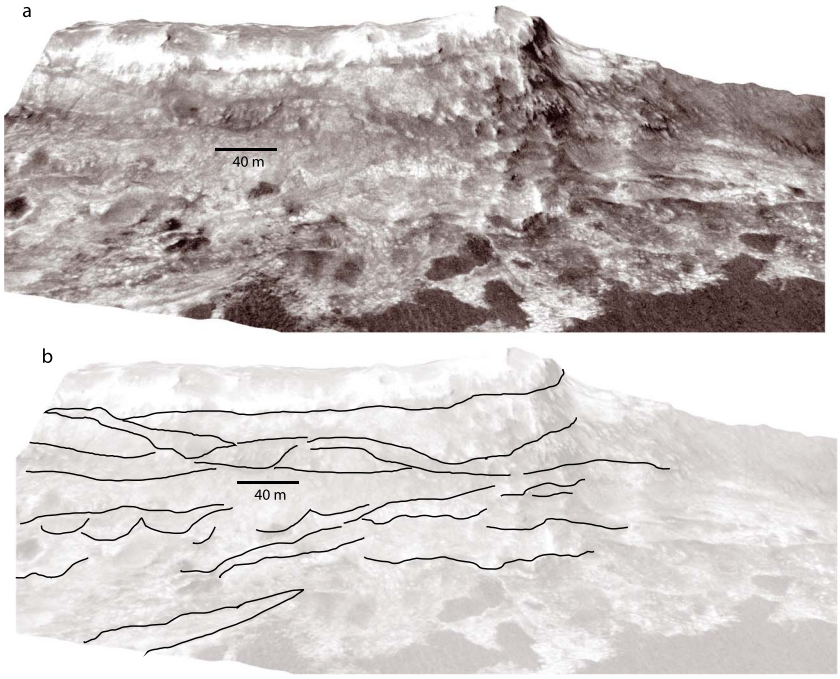

Figure 20. Large concave-up structures are reminiscent of paleochannels or convoluted bedding (a-b). HiRISE image is DTEEC_007599_2020_007454_2020_U01.

younger units encroached from the south and east. The uppermost portions of the central basin deposits grade into and/or are interbedded with the Keren ejecta deposits.

The Keren impact event produced the ~25-km diameter Keren impact crater, which includes mapped crater floor and central peak materials (krf) as well as Keren *crater wall and rim materials* (krw). The ejecta from Keren crater (ke) were deposited on the plains outside of McLaughlin crater as well as within the

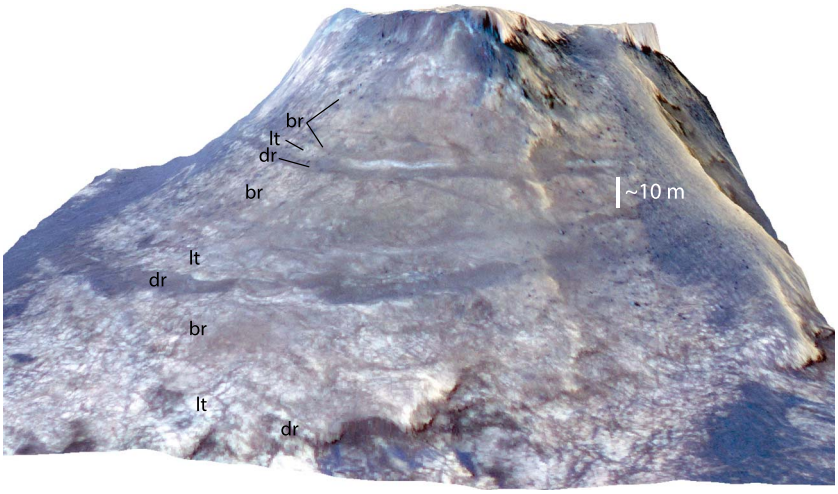

Figure 21. HiRISE false color (IRB) data draped over HiRISE DEM data show and eroded butte in the central part of the canyon. Note the packages of three units including an upper false color-brown unit (marked "br") (a), a thinner, middle false color light-toned unit (marked "lt") (b), and a lower, thin, darker false-color dark-toned unit (mark3ed "dr") (c). The solution to a three-point problem on these beds indicates a shallow (<3–5°) SW dip (255). HiRISE image is PSP_007454_2020_COLOR. HiRISE = High-Resolution Imaging Science Experiment.

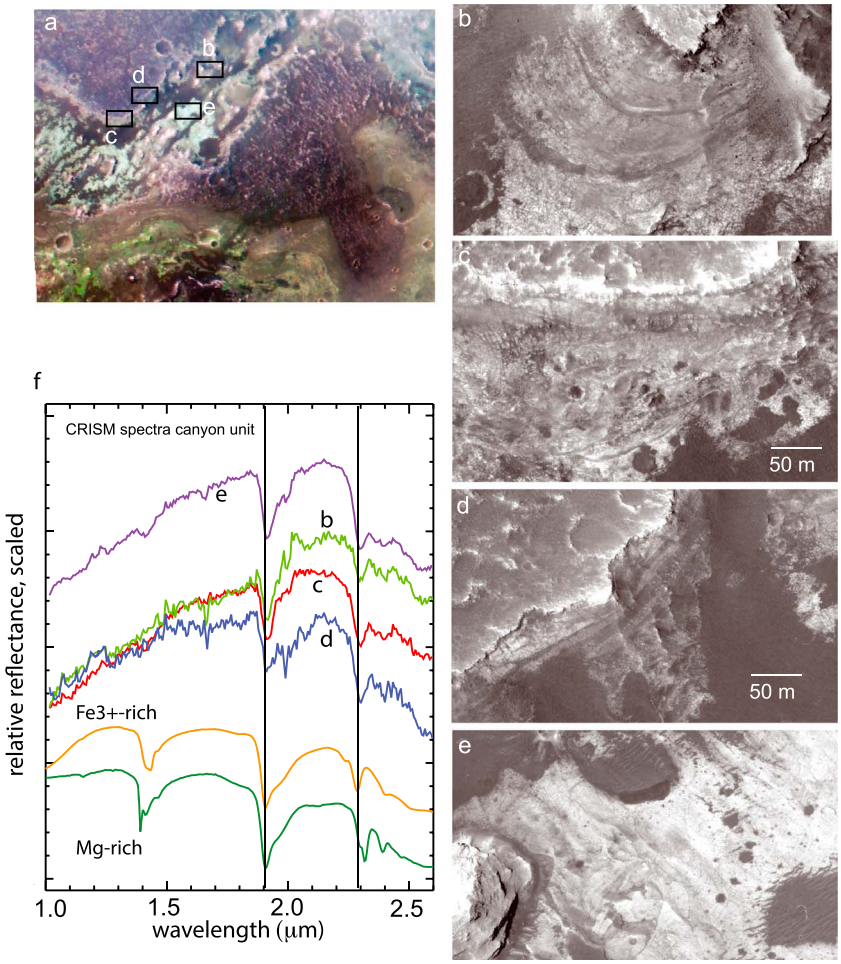

Figure 22. CRISM infrared spectra of the walls and floor of the canyon show clear evidence for Fe-rich clay minerals. A false color image shows the clay occurrences in light blue hues (R, 2.38 μm; G, 1.80 μm; and B, 1.15 μm) (a). Strong absorptions at 1.41, 1.92, 2.3, 2.39, and 2.52 μm indicate the presence of Mg-bearing, Fe-rich dioctahedral clay minerals similar to seafloor nontronites (b). HiRISE views of the surfaces from where spectra were extracted show bedding structures of the clay-bearing deposits. CRISM image is FRTA5AA. CRISM = Compact Reconnaissance Imaging Spectrometer for Mars; HiRISE = High-Resolution Imaging Science Experiment.

McLaughlin crater basin. As described above and illustrated in Figures 9 and 10, these deposits have clearly different morphology and mineralogy in the two different contexts (in and outside of McLaughlin basin). While the Keren ejecta deposits within McLaughlin have been clearly modified and are therefore mapped as a different unit, the occurrence of the Keren ejecta throughout provides a useful time-stratigraphic marker unit used in the next section to constrain absolute ages. The *south basin unit* (sbu) is the modified part of the Keren ejecta deposited within McLaughlin basin. As described above, these materials are composed of serpentinized bedrock containing carbonate veins, clay-bearing debris flow deposits, and layered, multicolored altered ejecta layers.

In the east side of McLaughlin crater basin are the *east basin deposits* (ebd) and *platform sedimentary deposits* (ps). The east basin deposits are a suite of shallowly SW dipping, layered, light-toned clay-bearing, deposits. The basal portion of this unit appears to be a gradational contact with the underlying central basin deposits. The platform sedimentary deposits are a suite of clay-bearing bottomsets, foresets, and topsets. The topmost and easternmost parts of this unit are composed of topsets built by and eroded by western migration of channels into the delta. The platform sediments are likely contemporaneous with the east basin deposits, which may represent deep-water fan deposits.

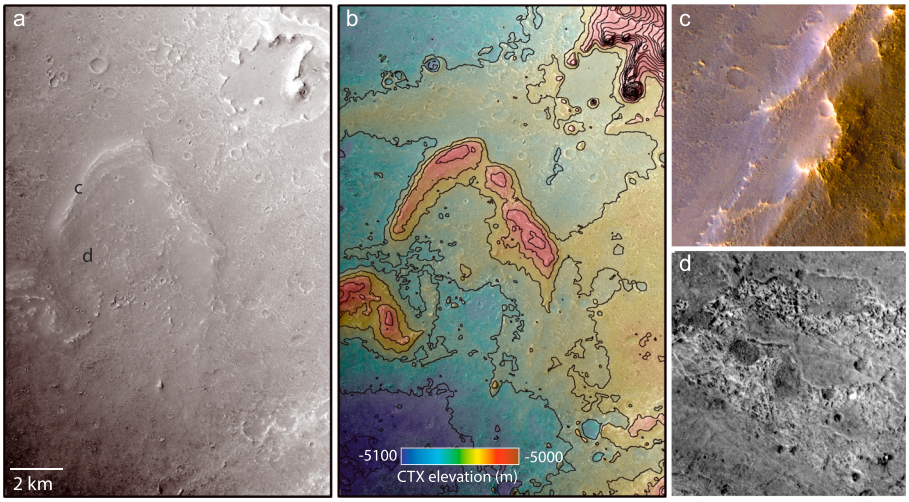

Figure 23. Lobate deposits occur within the central McLaughlin crater floor. CTX data show the multiple lobes, which appear convex north in plan view (a). Though the deposits are mantled by dark materials, it is clear that they are layered materials. CTX Digital Terrain Model (DTM) data show that the northernmost arcuate edges of the deposits rise as much as 40 m above the surrounding terrain (b) (CTX data have a 10-m contour interval). HiRISE data of the edge of the lobate materials shows colluvial material that has eroded out of layers and also illustrates that the deposit does not form cliffs resistant to erosion (c). Though the unit is poorly exposed, erosional windows into the stratigraphically highest parts of the deposits reveal dense networks of irregular, narrow ridges (d) similar to those observed in the east deposits (in Figure 16c). HiRISE images are ESP_037149_2020_RED and ESP_037149_2020_COLOR. HiRISE = High-Resolution Imaging Science Experiment; CTX = Context Imager.

The south, central, and western parts of McLaughlin basin contain interesting landslide and lobate deposits. Landslide deposits (ls) in the south include large segments of the south basin unit that have been modified by mass movements as illustrated in Figure 25. These northward flowing landslides appear genetically and temporally linked to *lobate debris flows* (df) observed in the central basin (Figures 23 and 24). Given their geologic context, mineralogy, bedding runout distance, and stratigraphic constraints, these deposits are interpreted as deep-water density currents or turbidites.

Two relatively younger units are mapped. In some places, relatively younger (though still ancient) impact craters (5- to 10-km diameter) have modified target rocks and obfuscated contact relations too strong to be mapped as the target unit. These materials are mapped as undifferentiated *crater materials* (cm).

The youngest of the mapped units is the dark *mantling material* (dm). As described above and illustrated in Figure 27, these include a range of draping, dark, eolian, and volcanoclastic materials. They are pyroxene bearing, locally olivine rich, and generally unaltered (compared to the other basin units). These materials postdate the McLaughlin crater lake and provide another key time-stratigraphic marker unit (Noe Dobrea et al., 2010).

3.2.8. Geology of the Basin: Timing and Stratigraphic Relations

To constrain absolute ages of geologic units and events in the McLaughlin basin, we produced crater size frequency statistics. The technique requires identification and counting of impact craters in clearly delineated areas that correspond to geologically sensible units. In other words, craters were counted within polygons that correspond to mapped units.

Datable time-stratigraphic markers are noted with stars in the geologic map and illustration of relative ages (Figure 32). A straightforward application of crater age dating is therefore the application to the deposition of the dark mantling units as this material postdates the lake, is fairly easily datable, and therefore provides a key constrain on the latest possible date that the lake existed. Analysis of 48 craters within the dark unit on the basin floor suggests that this material has been exposed for ~3.7 Gyr (Figure 34).

A second datable time-stratigraphic marker unit is the Keren ejecta blanket, both altered and unaltered. Treating the unaltered and altered Keren ejecta (units ke and sbd) as a single polygon, craters were

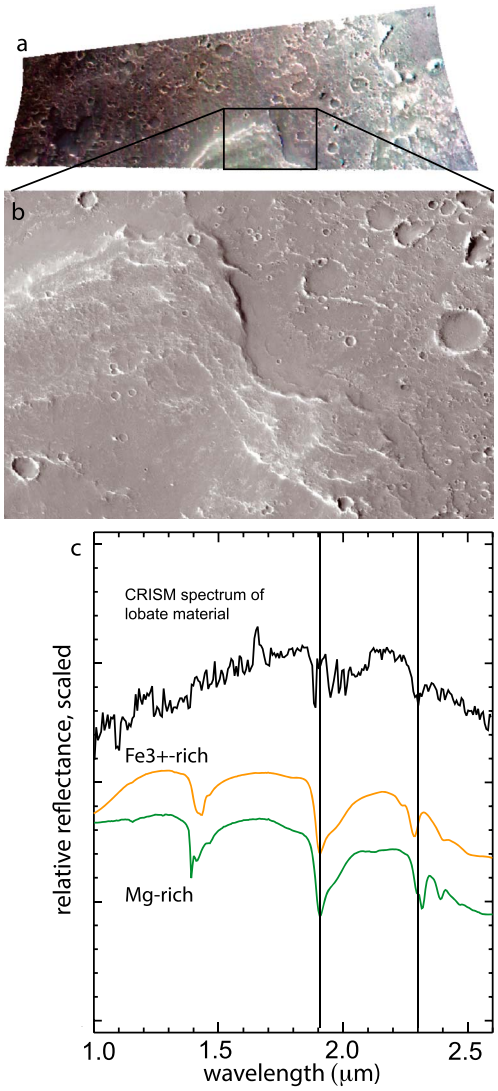

Figure 24. (a) False color CRISM image (R, 2.38 μm; G, 1.80 μm; and B, 1.15 μm). CRISM infrared spectra of the eroded edge of the lobate deposits display a 2.3-μm feature consistent with the presence of Fe-rich, Mg-bearing clay minerals, as observed in the east deposits. These CRISM data are noisy because they were collected after the failure of one cryocooler. CRISM image is FRS2EF79. CRISM = Compact Reconnaissance Imaging Spectrometer for Mars.

counted throughout the unit to constrain minimum age of the impact event. Counting of 39 craters in this unit suggests a minimum age of ~3.8 Ga (Figure 33).

Lastly, an attempt was made to constrain the age of the McLaughlin impact itself. This is a challenge because the basin is obviously quite ancient, and in order to apply the technique to very ancient structures, large counting polygons are required because counting of ancient surfaces requires counting of populations of relatively large craters. This problem was constrained by delineating a circular polygon centered on the center point of McLaughlin crater and extending out to one crater diameter from the crater rim. This is a reasonable distance in which Mclaughlin ejecta would be delineated if it were deposited onto older craters. Of course, it is impossible to rule out the possibility that McLaughlin's ejecta were deposited and subsequently removed by erosion while preserving the morphology of other local craters, but this is unlikely. Therefore, craters occurring within McLaughlin crater and those superimposed on its theoretical zone of ejecta were counted to constrain the formation age of the impact. In this case, that estimate is ~4.1 Ga, based on counting of 13 craters (Figure 33).

4. Synthesis and Discussion

4.1. Geologic History of McLaughlin Crater

The 92-km-diameter McLaughlin impact crater likely formed in the Early Noachian circa 4.1 Ga (Figure 34). An impact of this size would have resulted in pervasive faults and fractures within the target terrain, as well as the deposition of a melt sheet and breccia. The heat deposited from an impact of this size on Mars would have resulted in a hydrothermal system fueled by groundwater for ~10^5–10^6 years (Abramov & Kring, 2005) that could have altered much of the fractured bedrock within the crater floor and lower parts of the basin walls. This material would generally be poorly exposed, with the exception of blocks in landslides, discussed further below.

Sometime between the formation of McLaughlin crater and the formation of Keren crater circa 3.8 Ga, a lake existed in the basin (Figure 34). Layered, clay-rich lacustrine sedimentary rocks in the floor of the crater underlie ejecta from Keren and therefore a lake existed prior to the formation of Keren. There is no way to constrain the duration of the lake's existence. However, the ejecta from Keren that is located inside McLaughlin crater where the lake existed were also intensely altered by while the rest of the ejecta were not substantially altered. Therefore, it must be that a lake also existed in McLaughlin crater after the Keren impact event. Evidence for turbidite sequences on the basin floor discussed below is consistent with the seismic effects of and deposition from a large impact crater on the edge of the McLaughlin lake, which is consistent with the presence of a lake in McLaughlin crater at the time when the Keren impact occurred. Therefore, alteration in the basin both predates and postdates the Keren impact event.

Large portions of serpentinized bedrock within the south basin deposits could have formed in at least three ways. First, serpentinization might have occurred in the subsurface within the wall of McLaughlin crater and later been exposed and deposited by mass wasting. The observed landslides originating from the southern wall of McLaughlin may have formed because the wall rock was fractured and intensely altered. Second the serpentine-bearing rocks might represent mineralization by hydrothermal springs within the floor of McLaughlin crater lake. Heat deposited by the Keren impact would likely have resulted in hydrothermally altered bedrock below Keren, altering rock within the southern wall of

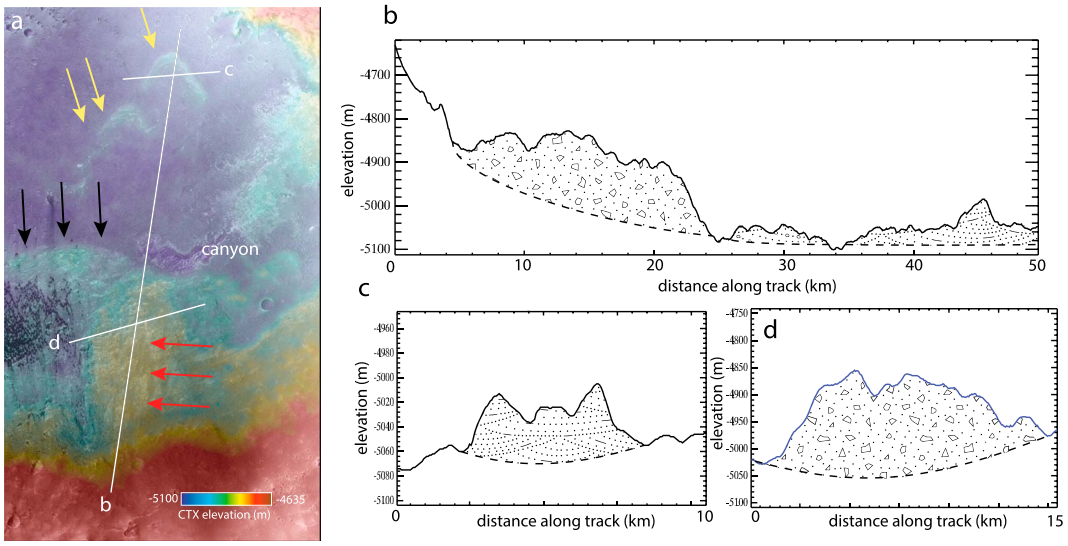

Figure 25. (a) HRSC topography data are draped over HRSC image data flows shown in Figure 24 are seen here in the north-central part of the image. These lobate materials are on trend with elongate, topographically high materials originating through collapse of the south basin deposits. HRSC topographic profiles are shown for three transects through the lobate materials. A landslide may have triggered a deep-water gravity flow that is tens of kilometers long and tens of meters thick. Black arrows point to the edge of Keren ejecta, red arrows point to a landslide deposit, and yellow arrows point to lobate materials, as referred to in the text. HRSC image is H5271_0000. HRSC = High-Resolution Stereo Camera.

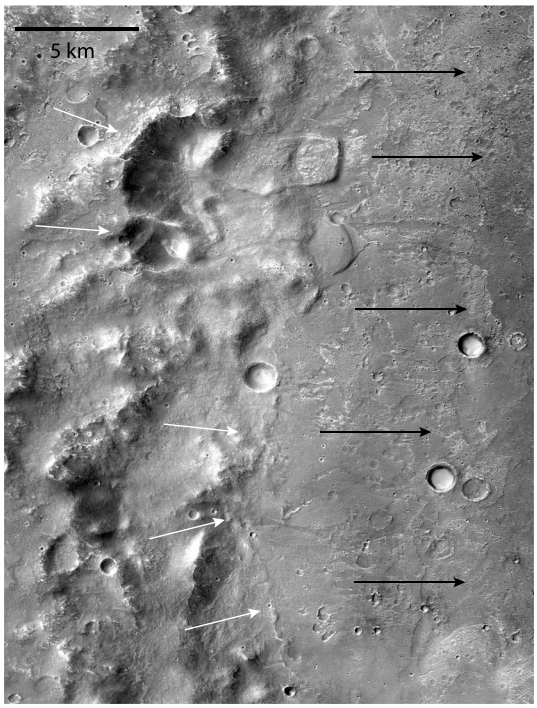

Figure 26. CTX image of landslide deposits in the west side of McLaughlin crater. Arcuate and sublinear scarps occur within the lower parts of the crater wall (white arrows). Thin (tens of meters) landslide deposits flowed eastward (black arrows) for ~5–10 km. CTX image is B17_016183_2014_XN_21N023W. CTX = Context Imager.

McLaughlin and potentially instigating the formation of spring-fed channels observed emanating from the south wall. A third possibility is that the serpentine is a type of chemical sediment formed in the bottom of a lake with ultramafic terrain that was rich in Mg^{2+} and low in dissolved silica. Such Mg-rich, alkaline lake environments on Earth tend to be silica-rich, resulting in precipitation of trioctahedral smectites. But if the solutions were silica limited in McLaughlin lake, it is possible that serpentine precipitated directly from lacustrine solution (Birsoy, 2002). This hypothesis might be less consistent with the identification of serpentine within intact bedrock blocks (Figures 15b and 15c) but entirely consistent with the occurrence of serpentine in layered soft sediments (Figures 15d and 15e).

The lake in McLaughlin crater existed after the Keren impact long enough to alter the ejecta materials, though the duration is difficult to constrain. The altered ejecta from Keren appear to be stratigraphically equivalent with lower parts of the east basin deposits, which are hundreds of meters thick. One hundred meters of sediments might have accumulated in ~1 × 10^5 years under modest sedimentation rates (Valpola & Ojala, 2006).

Strong evidence points to a base level having existed at an average elevation of −4,630 m, which implies that the lake would have been ~500-m deep. Though the lake level likely fluctuated, it is probable that lacustrine deposits in the deep basin represent deep-water, fine-grained detritus and chemical precipitates. Moving up in section and eastward in the basin, the sedimentary rocks likely contain an increasing fraction of clastic material.

An unaltered dark mantling unit draping the crater floor sediments, likely to be a volcanic ash fall, is dated to 3.6–3.7 Ga (Loizeau et al., 2012). This mantling unit is spectrally and geomorphologically similar to dark

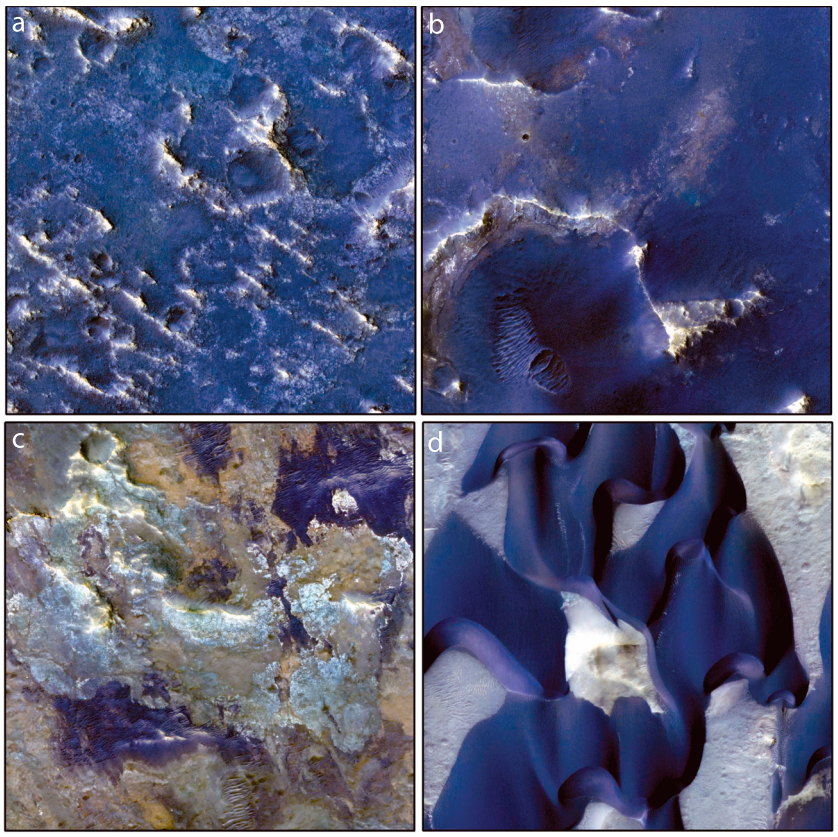

Figure 27. A relatively thin deposit of dark-toned material blankets the floor of McLaughlin crater at an average elevation of approximately −5,100 m (a). Similar deposits are seen draping rough terrain in the south basin deposits at higher elevations (−4,900 m) (b), suggesting an origin of the draping materials by airfall. At least two other types of dark materials are observed. Eroded patches of olivine-rich dunes (as revealed by CRISM) are found in the south basin deposits (c). Fields of younger barchan dunes are also observed (d). HiRISE images include PSP_007454_2020_COLOR, ESP_042991_2020_COLOR, and ESP_026666_2020_COLOR. CRISM = Compact Reconnaissance Imaging Spectrometer for Mars.

mantling deposits described in the Mawrth Vallis region, approximately 100 km to the east (Loizeau et al., 2010; Michalski & Fergason, 2009) and throughout other parts of the northwest Arabia Terra (Noe Dobrea et al., 2010). The dark mantle in McLaughlin crater is likely part of the same unit and overlies eroded portions of the crater floor, suggesting that late stage fluvial or eolian erosion had ceased and McLaughlin lake was permanently dry by ~3.7 Ga.

The nature of the late stage erosional processes has some unresolved aspects. The canyon in the floor of the basin formed during erosion of the crater floor materials to a depth of ~70–100 m. This should have resulted in the subsequent deposition of approximately several cubic kilometers of material by fluvial or colluvial processes, but there is no obvious sign of these in the basin and there is no outlet through which material could have been transported. It is otherwise hypothesized that the basin floor deposits would have been composed of very fine grained sediments. Eolian erosion and transport of fine-grained materials might have removed basin floor materials in suspension.

4.2. Astrobiology of McLaughlin Crater Lake

Astrobiology is one of the key drivers in Mars exploration, and the age and nature of the aqueous processes hosted in McLaughlin crater provide a number of potential opportunities to explore for clues to abiogenesis, evidence of prebiotic biosignatures, or evidence of life itself.

Perhaps the greatest value of this site is that McLaughlin crater contains not only a wide range of hydrothermal but also a wide range of sedimentary contexts relevant to energy availability, nutrient cycling, and the

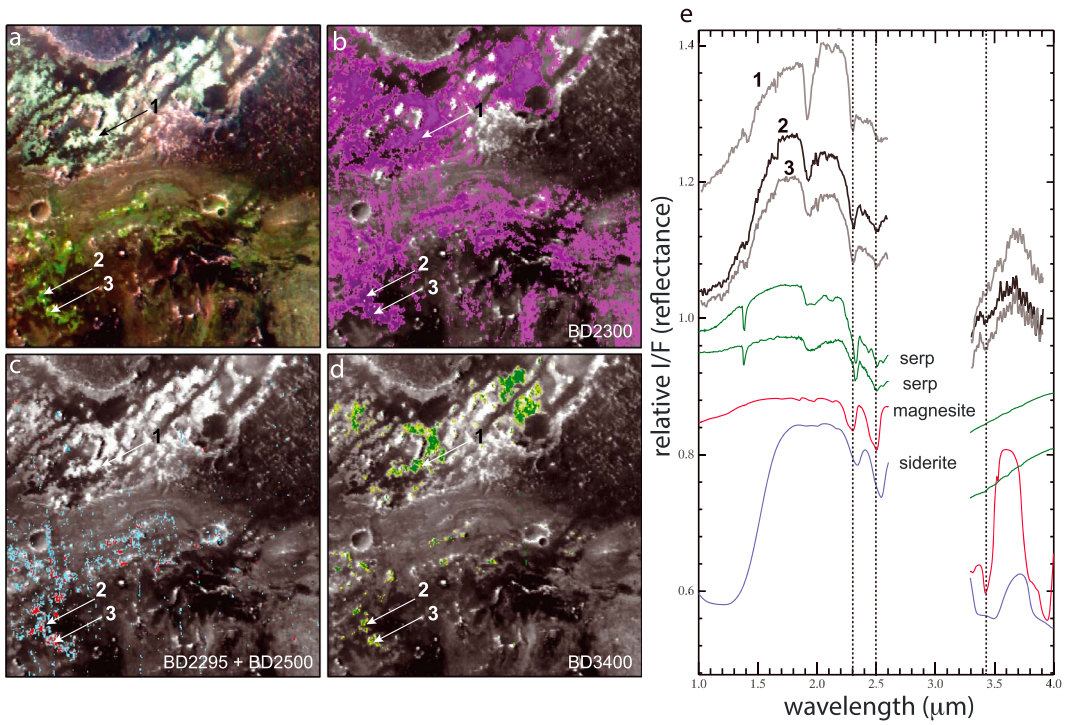

Figure 28. CRISM spectra are evaluated here to determine if serpentine, carbonate, or both are present in McLaughlin basin. (a) A CRISM false color image (R, 2.38 μm; G, 1.80 μm; and B, 1.15 μm) is shown for context; three locations where spectral ratio data were extracted are marked. (b) A CRISM parameter map BD2300 identifies minerals with an absorption near 2.3 μm. This is effective for Fe,Mg-clay minerals and also detects the C-O absorption in Mg-rich carbonates. (c) Two additional parameter maps: a 2.295-μm parameter (blue) that can be useful for detecting Mg carbonates and a 2.50-μm parameter (red) that also occurs in Mg-rich carbonates. (d) The 3.4-μm parameter map, which could indicate carbonates. The BD3400 maps are also sensitive to thermal effects, however. Extracted ratio spectra (e) show several important characteristics: (1) they are probably most spectrally similar to serpentine-group minerals in the 2.2- to 2.6-μm range, (2) the matches are not exact because the metal-OH features in serpentine in this range are affected by crystal chemistry, (3) C-O absorptions in magnesite have similar absorption maximum (reflectance minima) as those observed in the deposits, (4) some of the south basin deposits (spectra 2 and 3) have a 3.4-μm feature suggesting that magnesite is present and that serpentine is not sufficient to explain the data. In summary, both serpentine and Mg carbonate are likely required to explain the observations. CRISM image is FRTA5AA. CRISM = Compact Reconnaissance Imaging Spectrometer for Mars.

deposition and preservation of biosignatures. The highly diverse mineralogy suggests that multiple chemical gradients existed in the lacustrine environment, providing life with several potential energy-harvesting metabolic pathways.

Detailed spectroscopy of the lake floor provides clues to the chemistry and chemical gradients present. Strong hydroxyl absorptions at 2.295 μm are most consistent with dioctahedral (Fe^{3+}) clays that contain abundant substitution by Mg^{2+} and/or Fe^{2+} (Michalski et al., 2015, see spot 1 in Figures 28 and 29, for example). A steep spectral slope observed between ~1.3 and 1.6 μm is likely indicative that Fe^{2+} is present in the clay. The presence of ferrihydrite in sediments that probably formed in a reducing environment is particularly intriguing because it might indicate the presence of some oxidation process out of equilibrium with the setting. It is noted that only minor sulfate minerals are detected, which could indicate the unlikely case that sulfur is very low or absent, or that sulfur is primarily present in reduced forms that are difficult to detect remotely. The range of conditions implied by these observations suggests that the pH was probably not excessively low and that abundant energy sources were available for Fe-reducing, Fe or H-oxidizing bacteria or methanogens, or other life.

Evidence for serpentine is strong and unambiguous, and it is well known that serpentinization reactions acting on mafic and ultramafic crust result in abundant H_2 production and alkaline conditions (Martin et al.,

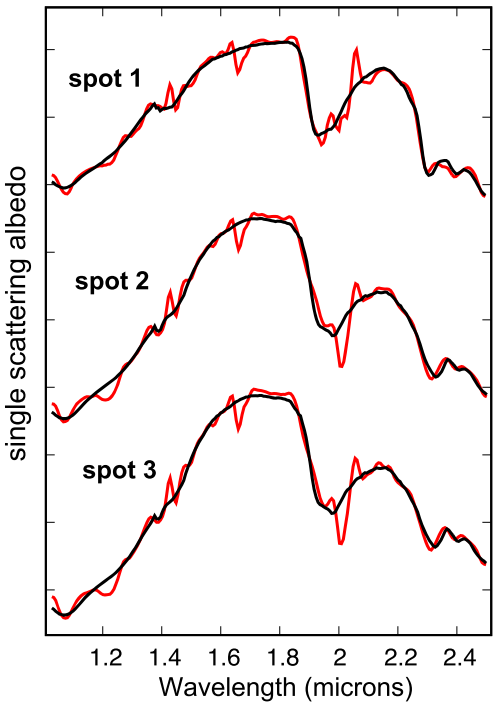

Figure 29. CRISM spectra (red) are shown for each of the three spots in Figure 28 along with modeled spectra (black) in units of single-scattering albedo (SSA). Each of the spectra was scaled to lower spectral contrast; the actual maximum SSA for each spectrum is ~0.62 and the absolute spectral contrast of the 1.9-μm feature is ~ 0.05. Spots 2 and 3 were also offset for clarity but have similar characteristics. CRISM image is FRTA5AA. CRISM = Compact Reconnaissance Imaging Spectrometer for Mars.

2008). In addition, because carbonates are also found in the lake, it can be concluded that CO_2 present in the system would have led to production of CH_4. Either H_2 or CH_4 could have provided abundant energy for chemosynthetic organisms. Even if life did not originate on Mars, evidence of prebiotic chemistry may nevertheless be preserved in McLaughlin basin.

Likewise, the varied sedimentary processes that occurred in McLaughlin crater could have provided important means for preserving potential biosignatures. The occasional occurrence of turbidites would have also resulted in the rapid burial of lake-floor sediments, and possibly the entrainment of lake-floor hydrothermal spring deposits, if they existed. Rapid burial and entombment of biosignatures would mean that the floor of McLaughlin lake is a target-rich environment for preservation of organic matter. In the absence of grazing organisms, a deep-water, calm, reducing environment may have allowed for the deposition and sequestration of organics and other molecular biosignatures.

A lake possibly existed in McLaughlin crater at or before the time of the demise of a strong Martian core dynamo, estimated by coarse-resolution magnetic field data to be ~3.9–4.1 Ga. This radiation shielding could have been beneficial as the lake first formed and through time along shallow shorelines, where redox gradients at the sediment-water interface may have also provided favorable energetics for life.

Yet the habitability of McLaughlin lake, unlike many shallow aqueous environments on Mars, likely persisted long beyond the cessation of Mars' protective Martian magnetic field. Even if the surface of Mars was bombarded by high-energy radiation by the time McLaughlin lake existed, the substantial connections between the surface and the deep-water environment would have allowed possible biological organisms a pathway to remain protected from these deleterious surface conditions. Even if the surface conditions were oxidizing, the deep-water (hundreds of meters) environment in McLaughlin lake would have likely sequestered sediments and potential organics away from destructive processes. These basin materials were likely always shielded from deleterious radiation such as ultraviolet rays, solar energetic particles, and galactic cosmic rays, which would most likely have only affected the uppermost meters of rock or

Table 1
Parameters Used to Model Spectra From CRISM Cube FRTA5AA

	Spot 1			Spot 2			Spot 3	
Component	Grain size (microns)	Abundance (%)	Component	Grain size (microns)	Abundance (%)	Component	Grain size (microns)	Abundance (%)
Augite	1200	25.2	Lizardite LALZ01	200	36	Lizardite LALZ01	200	32.6
Lizardite LALZ01	200	16.4	Augite	1200	26.4	Augite	1200	29.2
Ferrihydrite	100	16	Forsterite	300	13.2	Forsterite	300	14.9
Nontronite 612–614	10	11.6	Nontronite 612–614	10	7	Epsomite	15	5.5
Forsterite	75	10.5	Epsomite	15	6.4	Diopside	1200	5.4
Nontronite Nau-2	300	4.9	Diopside	1200	5.9	Nontronite 612–614	10	5.4
Vermiculite	300	4.5	Magnesite	150	1.7	Magnesite	150	1.7
Augite	50	3.6	Calcite	600	1.6	Kieserite	35	1.6
Epsomite	15	2.8	Kieserite	35	1.3	Calcite	600	1.3
Mars dust	50	2.7	Jarosite	300	0.4	Augite	75	0.9
Calcite	600	1	Dolomite	600	0.1	Jarosite	300	0.6

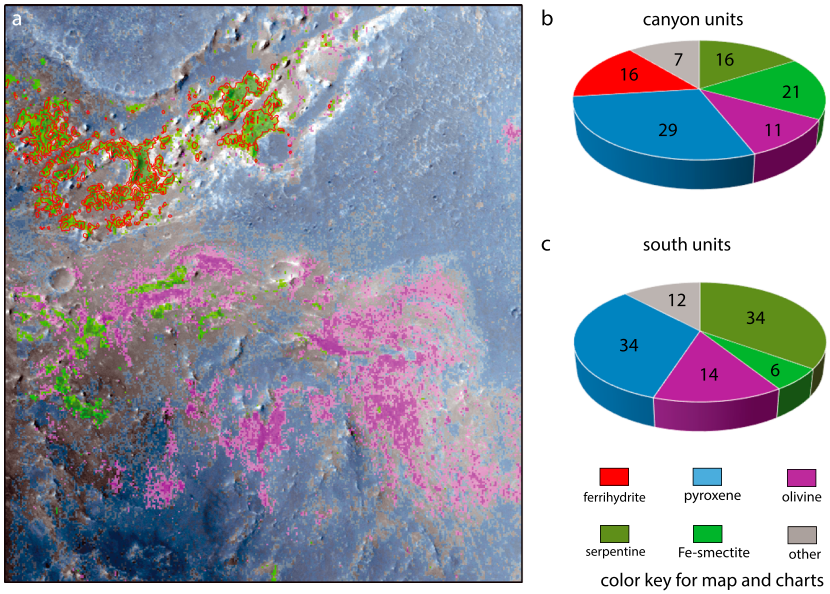

Figure 30. Mineral abundance maps showing the occurrence of oxides, clays, olivine, and pyroxene in the canyon sediments based on modeling of CRISM data. All mineral groups are shown as color raster overlays, except ferrihydrite, which is contoured. CRISM = Compact Reconnaissance Imaging Spectrometer for Mars.

several tens of meters of water/ice in the lake. Thus, McLaughlin crater may represent one of the longest continually habitable surface environments on Mars.

The specific contexts in which organic material could become incorporated into the sedimentary record in McLaughlin include: (a) layers in deep-water pelagic sediments, (b) bottomset and foreset sediments within spring-fed delta and fan deposits in the eastern part of the basin, (c) incorporation into turbidite materials, and (d) incorporation into landslide deposits. Hydrothermal deposits could

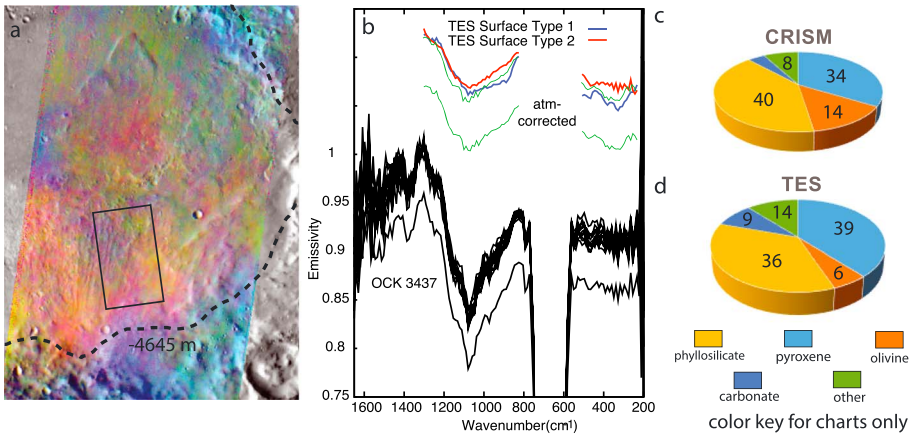

Figure 31. (a) A THEMIS DCS image. Bands 8, 7, and 5 are assigned to R, G, and B in this image. Blue-green hues correspond to more mafic materials that absorb more strongly at longer wavelengths (band 8). Red-yellow hues correspond to materials that absorb more strongly at short wavelengths (band 5), such as clay minerals. The dashed line corresponds to the putative lake level of −4,635 m; note the difference in composition below this elevation. The black box notes the location from where TES spectra where extracted (b). TES emissivity spectra, uncorrected for atmosphere, are shown below for orbiter counter (OCK) 3437. Multiple surface spectra, averaged and corrected for atmospheric effects, are shown above. The same spectrum is compared to TES surface types 1 and 2 at the top of Figure 31b. TES abundances are shown in a plagioclase-free space (i.e., normalized to zero plagioclase). CRISM = Compact Reconnaissance Imaging Spectrometer for Mars; THEMIS = Thermal Emission Imaging System; TES = Thermal Emission Spectrometer.

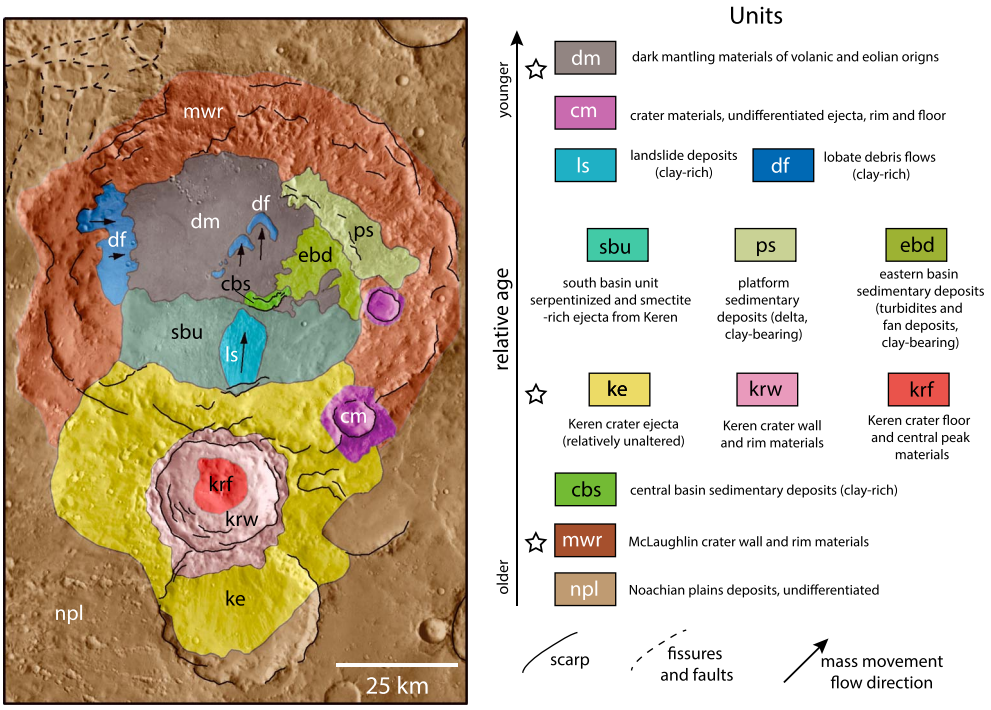

Figure 32. A geologic-geomorphic map of McLaughlin crater. Mapped units, from oldest to youngest are shown at the right. Units of similar age, or for which age relations are not differentiated, are shown in parallel rows. Stars indicate points in the relative chronology where crater counting is used to estimate absolute age markers. Scarps, fissures, and faults are noted. Arrows indicate the direction of mass movement as indicated by morphology of lobate deposits. Detailed unit descriptions are shown in the text.

contain biotextures in mineral replacements and vein fill or potentially evidence of life trapped in fluid inclusions and mineral waste products. In addition, all of the deposits could contain indirect bioindicators such as metal accumulations, sharp redox gradients, and isotopic variations requiring disequilibrium chemistry.

4.3. Terrestrial Analogs for McLaughlin Lake

Though there is no direct analog for McLaughlin lake on Earth, a number of geological features and deposits provide some insight into its geology and biological potential. At ~500-m depth and with a volume of

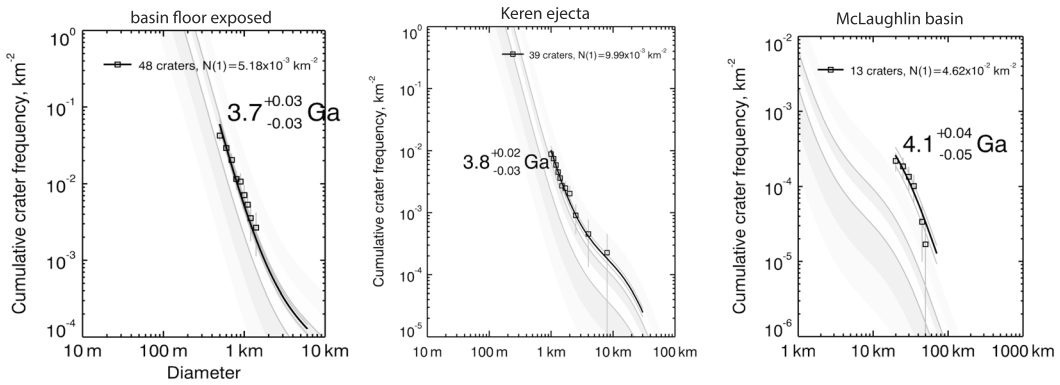

Figure 33. Cumulative crater frequency plots are shown along with model fits and isochrons for three units/events representing craters accumulate since the formation of McLaughlin crater (left), the deposition of Keren ejecta (center), and the exposure of the floor of McLaughlin crater (right).

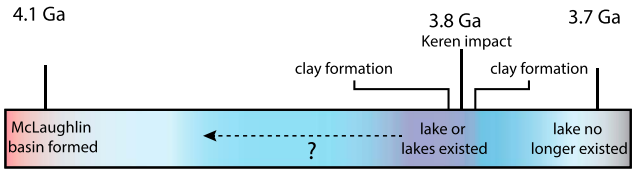

Figure 34. A timeline shows the timing of the occurrence of McLaughlin crater lake. The basin had formed by 4.1 Ga. Ejecta from Keren crater deposited circa 3.8 Ga overlie deep-water sediments and also were altered by significant water. Therefore, the lake existed either both before and after the Keren impact event, or perhaps more likely, the ejecta were deposited into the lake. Based on crater counts on the crater floor, the lake ceased to exist by ~3.7 Ga.

Figure 35. Issyk Kul is a modern high-altitude tectonic lake located in Kyrgyzstan with comparable area, depth, and volume to that of the ancient McLaughlin lake on Mars.

~1,500 km^3, McLaughlin lake would have been comparable in size and depth to Issyk Kul, a large, high-altitude lake in Kyrgyzstan (Aladin & Plotnikov, 1993, Figure 35). Though air temperature of Issyk Kul is below freezing during the winter months, the lake does not freeze because it is fed by hot springs and is mesosaline (6 g/L). Deep-water deposits in Issyk Kul include fine-grained carbonate-clay muds (hydrotalcite + poorly characterized clay minerals, Gómez-Paccard et al., 2012) as well authigenic sulfide and well-preserved organic matter (Rasmussen et al., 1998). Deep basin deposits in Issyk Kul also include turbidites formed in response to frequent seismicity in the region (Bowman et al., 2004). Though McLaughlin lake existed in an entirely different tectonic setting to Issyk Kul, frequent seismicity would be expected to have occurred on ancient Mars due to frequent meteor impact, and therefore, deep-water sediments might contain similar deposits.

The presence of turbidites in McLaughlin lake sediments is reasonable given the context. The fortuitous exposures of canyon walls in the McLaughlin basin floor provide unprecedented opportunities to observe Martian lake floor deposits in 3-D. Similarly, beach cliffs in the San Clemente, USA, region reveal amazing detail about the facies associated with certain turbidites on Earth (Camacho et al., 2002; Li et al., 2016) (Figure 36). The San Clemente deposits show a range of subaqueous channel and channel margin deposits displaying multiple erosion surfaces, multiple scales of laminations and bedding, dewatering structures, and convolute bedding related to soft-sediment deformation, all of which might provide insight into the process sedimentology accessible in McLaughlin crater.

Though significantly smaller in scale, another interesting analog for McLaughlin crater lake is Lonar crater lake in Maharashtra, India (Maloof et al., 2010). Lonar crater is one of the only impact craters on Earth that exists in basalt target rocks (Wright et al., 2011). Because the crater was recent (likely 50 Kyr but perhaps 500 Kyr), its morphology and geology is well preserved. In in the ~1.2-km crater basin is a ~1-km diameter, 10-m deep lake (Figure 37). The lake floor contains approximately tens of meters of sediments composed of poorly characterized clay minerals and metastable carbonates deposited on a basement of fractured and hydrothermally altered basalt (Hagerty & Newsom, 2003). Though only a small lake, Lonar contains a vast and interesting array of microbial life linked to multiple energy sources and environmental settings (Antony et al., 2013; Paul et al., 2016).

Figure 36. Field photos of turbidite deposits exposed in sea cliffs near San Clemente, California. Compare to bedding observed in cliff faces in McLaughlin crater shown in Figures 19 and 20. Image credit: Zoltan Sylvester.

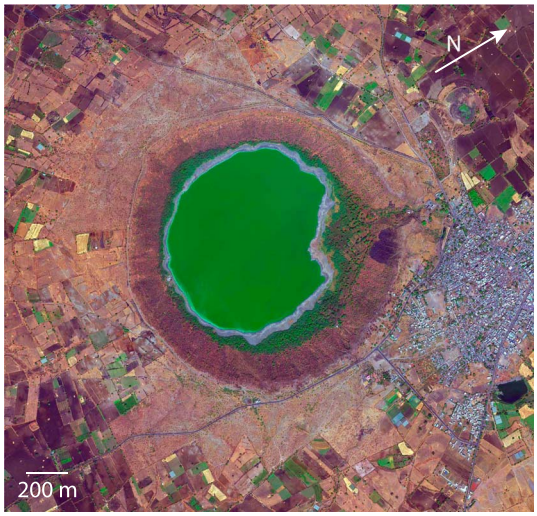

Figure 37. A Worldview 2 image of Lonar crater in India. Image is a true-color decorrelation stretched image draped over higher-resolution (40 cm) panchromatic data. Though it is>50 times smaller scale than McLaughlin crater, Lonar crater provides some insights into the properties of an alkaline, groundwater-fed lake in a mafic protolith.

5. Conclusions

McLaughlin crater formed from a large meteor impact >4 Ga. The resulting 92-km-diameter basin contains rocks recording a complex history of ancient lacustrine and hydrothermal processes. These include some of the most relevant deposits in the search for evidence of ancient biomarkers on Mars. The geology also contains exceptional examples of geologically important phenomena such as serpentinized crust, deep-water clay-carbonate mudrocks, delta and fan deposits, and the first evidence for turbidites on another planet.

In the Mid-Noachian (circa 3.8 Ga) McLaughlin crater basin contained a ~500-m-deep, voluminous and potentially long lived lake. This groundwater-fed lake would have been among the deepest and most voluminous to have existed on Mars at any point in the Noachian and may have been one of the longest continually habitable surface environments on Mars. Fluids in the spring-fed lake would have been rich in Fe^{2+}, Mg^{2+}, CO_2, H_2, and CH_4 that could have fueled a chemosynthetic biosphere. The presence of deep-water sediments containing various clay minerals as well as ferrihydrite might be an indication of disequilibrium in the lake, also deepening McLaughlin crater's appeal as a target for astrobiological exploration.

Acknowledgments
Nearly all data used in this research are available through the Planetary Data System (https://pds.nasa.gov/). These include remote sensing data from the Mars Express OMEGA and HRSC instruments, Mars Reconnaissance Orbiter CRISM, HiRISE, and CTX instruments, Mars Odyssey THEMIS instrument, and Mars Global Surveyor TES and MOLA instruments. A graphic interface to search for and obtain data is available using Arizona State University's JMARS free software (https://jmars.asu.edu/).

References

Abramov, O., & Kring, D. A. (2005). Impact-induced hydrothermal activity on early Mars. *Journal of Geophysical Research*, *110*, E12S09. https://doi.org/10.1029/2005JE002453

Achille, G. di, & Hynek, B. M. (2010). Deltas and valley networks on Mars. In N. A. Cabrol & E. A. Grin (Eds.), *Lakes on Mars*. (pp. 223–248). Amsterdan, Netherlands: Elsevier.

Aladin, N. V., & Plotnikov, I. S. (1993). Large saline lakes of former USSR: A summary review. *Hydrobiologia*, *267*(1-3), 1–12. https://doi.org/10.1007/BF00018787

Andrews-Hanna, J. C., Zuber, M. T., Arvidson, R. E., & Wiseman, S. M. (2010). Early Mars hydrology: Meridiani playa deposits and the sedimentary record of Arabia Terra. *Journal of Geophysical Research*, *115*, E06002. https://doi.org/10.1029/2009JE003485

Antony, C. P., Kumaresan, D., Hunger, S., Drake, H. L., Murrell, J. C., & Shouche, Y. S. (2013). Microbiology of Lonar lake and other soda lakes. *The ISME Journal*, *7*(3), 468–476. https://doi.org/10.1038/ismej.2012.137

Balme, M., Berman, D. C., Bourke, M. C., & Zimbelman, J. R. (2008). Transverse aeolian ridges (TARs) on Mars. *Geomorphology*, *101*(4), 703–720. https://doi.org/10.1016/j.geomorph.2008.03.011

Bandfield, J. L. (2002). Global mineral distributions on Mars. *Journal of Geophysical Research*, *107*(E6), 5042. https://doi.org/10.1029/2001JE001510

Bibring, J. P., Langevin, Y., Gendrin, A., Gondet, B., Poulet, F., Berthe, M., et al. (2005). Mars surface diversity as revealed by the OMEGA/Mars Express observations. *Science*, *307*(5715), 1576–1581. https://doi.org/10.1126/science.1108806

Birsoy, R. (2002). Formation of sepiolite-palygorskite and related minerals from solution. *Clays and Clay Minerals*, *50*(6), 736–745. https://doi.org/10.1346/000986002762090263

Bowman, D., Korjenkov, A., & Porat, N. (2004). Late-Pleistocene seismites from Lake Issyk-Kul, the Tien Shan range, Kyrghyzstan. *Sedimentary Geology*, *163*(3-4), 211–228. https://doi.org/10.1016/S0037-0738(03)00194-5

Brown, A. J., Hook, S. J., Baldridge, A. M., Crowley, J. K., Bridges, N. T., Thomson, B. J., et al. (2010). Hydrothermal formation of clay-carbonate alteration assemblages in the Nil fossae region of Mars. *Earth and Planetary Science Letters*, *297*(1-2), 174–182. https://doi.org/10.1016/j.epsl.2010.06.018

Camacho, H., Busby, C. J., & Kneller, B. (2002). A new depositional model for the classical turbidite locality at San Clemente State Beach, California. *AAPG Bulletin*, *86*. https://doi.org/10.1306/61EEDCF6-173E-11D7-8645000102C1865D

Carr, M. H., & Clow, G. D. (1981). Martian channels and valleys: Their characteristics, distribution, and age. *Icarus*, *48*(1), 91–117. https://doi.org/10.1016/0019-1035(81)90156-1

Carr, M. H., & Head, J. W. (2010). Geologic history of Mars. *Earth and Planetary Science Letters*, *294*(3–4), 185–203. https://doi.org/10.1016/j.epsl.2009.06.042

Christensen, P. R., Bandfield, J. L., Hamilton, V. E., Ruff, S. W., Kieffer, H. H., Titus, T. N., et al. (2001). Mars Global Surveyor Thermal Emission Spectrometer experiment: Investigation description and surface science results. *Journal of Geophysical Research*, *106*(E10), 23,823–23,871. https://doi.org/10.1029/2000JE001370

Christensen, P. R., Engle, E., Anwar, S., Dickenshied, S., Noss, D., Gorelick, N., & Weiss-Malik, M. (2009). JMARS—A planetary GIS. In *American Geophysical Union, Fall Meeting* 2009.

Christensen, P. R., Fergason, R. L., Edwards, C. S., & Hill, J. (2013). THEMIS-derived thermal inertia mosaic of Mars: Product description and science results. 44th Lunar and Planetary Science Conference. https://doi.org/10.1029/2006JE002735

Edwards, C. S., Bandfield, J. L., Christensen, P. R., & Fergason, R. L. (2009). Global distribution of bedrock exposures on Mars using THEMIS high-resolution thermal inertia. *Journal of Geophysical Research*, *114*, E11001. https://doi.org/10.1029/2009JE003363

Edwards, C. S., Bandfield, J. L., Christensen, P. R., & Rogers, A. D. (2014). The formation of infilled craters on Mars: Evidence for widespread impact induced decompression of the early Martian mantle? *Icarus*, *228*, 149–166. https://doi.org/10.1016/j.icarus.2013.10.005

Edwards, C. S., Nowicki, K. J., Christensen, P. R., Hill, J., Gorelick, N., & Murray, K. (2011). Mosaicking of global planetary image datasets: 1. Techniques and data processing for Thermal Emission Imaging System (THEMIS) multi-spectral data. *Journal of Geophysical Research*, *116*, E10008 https://doi.org/10.1029/2010JE003755

Ehlmann, B. L., Mustard, J. F., Fassett, C. I., Schon, S. C., Head, J. W. III, Des Marais, D. J., et al. (2008). Clay minerals in delta deposits and organic preservation potential on Mars. *Nature Geoscience*, *1*(6), 355–358. https://doi.org/10.1038/ngeo207

Ehlmann, B. L., Mustard, J. F., & Murchie, S. L. (2010). Geologic setting of serpentine deposits on Mars. *Geophysical Research Letters*, *37*, L06201. https://doi.org/10.1029/2010GL042596

Ehlmann, B. L., Mustard, J. F., Murchie, S. L., Poulet, F., Bishop, J. L., Brown, A. J., et al. (2008). Orbital identification of carbonate-bearing rocks on Mars. *Science*, *322*(5909), 1828–1832. https://doi.org/10.1126/science.1164759

Fassett, C. I., & Head, J. W. (2008). Valley network-fed, open-basin lakes on Mars: Distribution and implications for Noachian surface and subsurface hydrology. *Icarus*, *198*(1), 37–56. https://doi.org/10.1016/j.icarus.2008.06.016

Gillespie, A. R., Kahle, A. B., & Walker, R. E. (1986). Color enhancement of highly correlated images. I. Decorrelation and HSI contrast stretches. *Remote Sensing of Environment*, *20*(3), 209–235. https://doi.org/10.1016/0034-4257(86)90044-1

Gómez-Paccard, M., Larrasoaa, J. C., Giralt, S., & Roberts, A. P. (2012). First paleomagnetic results of Mid-to Late Holocene sediments from Lake Issyk-Kul (Kyrgyzstan): Implications for paleosecular variation in central Asia. *Geochemistry, Geophysics, Geosystems*, *13*, Q03019. https://doi.org/10.1029/2011GC004015

Goudge, T. A., Aureli, K. L., Head, J. W., Fassett, C. I., & Mustard, J. F. (2015). Classification and analysis of candidate impact crater-hosted closed-basin lakes on Mars. *Icarus*, *260*, 346–367. https://doi.org/10.1016/j.icarus.2015.07.026

Goudge, T. A., Mohrig, D., Cardenas, B. T., Hughes, C. M., & Fassett, C. I. (2018). Stratigraphy and paleohydrology of delta channel deposits, Jezero crater, Mars. *Icarus*, *301*, 58–75. https://doi.org/10.1016/j.icarus.2017.09.034

Hagerty, J. J., & Newsom, H. E. (2003). Hydrothermal alteration at the Lonar Lake impact structure, India: Implications for impact cratering on Mars. *Meteoritics & Planetary Science*, *38*(3), 365–381. https://doi.org/10.1111/j.1945-5100.2003.tb00272.x

Hapke, B. (1999). Scattering and diffraction of light by particles in planetary regoliths. *Journal of Quantitative Spectroscopy and Radiative Transfer*, *61*(5), 565–581. https://doi.org/10.1016/S0022-4073(98)00042-9

Hartmann, W., & Neukum, G. (2001). Cratering chronology and the evolution of Mars. *Space Science Reviews*, *96*(1/4), 165–194. https://doi.org/10.1023/A:1011945222010

Horgan, B. H. N., Cloutis, E. A., Mann, P., & Bell, J. F. (2014). Near-infrared spectra of ferrous mineral mixtures and methods for their identification in planetary surface spectra. *Icarus*, *234*, 132–154. https://doi.org/10.1016/j.icarus.2014.02.031

Irwin, R. P., & Zimbelman, J. R. (2012). Morphometry of Great Basin pluvial shore landforms: Implications for paleolake basins on Mars. *Journal of Geophysical Research*, *117*, E07004. https://doi.org/10.1029/2012JE004046

Ivanov, B. A. (2001). Mars/Moon cratering rate ratio estimates. *Space Science Reviews*, *96*, 87–104. https://doi.org/10.1023/A:1011941121102

Kneissl, T., Van Gasselt, S., & Neukum, G. (2011). Map-projection-independent crater size-frequency determination in GIS environments—New software tool for ArcGIS. *Planetary and Space Science*, *59*, 1243–1254. https://doi.org/10.1016/j.pss.2010.03.015

Li, P., Kneller, B. C., Hansen, L., & Kane, I. A. (2016). The classical turbidite outcrop at San Clemente, California revisited: An example of sandy submarine channels with asymmetric facies architecture. *Sedimentary Geology*, *346*, 1–16. https://doi.org/10.1016/j.sedgeo.2016.10.001

Liu, Y., Glotch, T. D., Scudder, N. A., Kraner, M. L., Condus, T., Arvidson, R. E., et al. (2016). End-member identification and spectral mixture analysis of CRISM hyperspectral data: A case study on southwest Melas Chasma, Mars. *Journal of Geophysical Research: Planets.*, *121*, 2004–2036. https://doi.org/10.1002/2016JE005028

Loizeau, D., Mangold, N., Poulet, F., Ansan, V., Hauber, E., Bibring, J. P., et al. (2010). Stratigraphy in the Mawrth Vallis region through OMEGA, HRSC color imagery and DTM. *Icarus*, *205*(2), 396–418. https://doi.org/10.1016/j.icarus.2009.04.018

Loizeau, D., Werner, S. C., Mangold, N., Bibring, J. P., & Vago, J. L. (2012). Chronology of deposition and alteration in the Mawrth Vallis region, Mars. *Planetary and Space Science*, *72*, 31–43. https://doi.org/10.1016/j.pss.2012.06.023

Maloof, A. C., Stewart, S. T., Weiss, B. P., Soule, S. A., Swanson-Hysell, N. L., Louzada, K. L., et al. (2010). Geology of Lonar crater, India. *Geological Society of America Bulletin*, *122*(1–2), 109–126. https://doi.org/10.1130/B26474.1

Martin, W., Baross, J., Kelley, D., & Russell, M. J. (2008). Hydrothermal vents and the origin of life. *Nature Reviews Microbiology*, *6*(11), 805–814. https://doi.org/10.1038/nrmicro1991

Michael, G. G., & Neukum, G. (2010). Planetary surface dating from crater size-frequency distribution measurements: Partial resurfacing events and statistical age uncertainty. *Earth and Planetary Science Letters*, *294*(3–4), 223–229. https://doi.org/10.1016/j.epsl.2009.12.041

Michalski, J., & Fergason, R. (2009). Composition and thermal inertia of the Mawrth Vallis region of Mars from TES and THEMIS data. *Icarus*, *199*(1), 25–48. https://doi.org/10.1016/j.icarus.2008.08.016

Michalski, J. R., Cuadros, J., Bishop, J. L., Darby Dyar, M., Dekov, V., & Fiore, S. (2015). Constraints on the crystal-chemistry of Fe/Mg-rich smectitic clays on Mars and links to global alteration trends. *Earth and Planetary Science Letters*, *427*, 215–225. https://doi.org/10.1016/j.epsl.2015.06.020

Michalski, J. R., Cuadros, J., Niles, P. B., Parnell, J., Rogers, A. D., & Wright, S. P. (2013). Groundwater activity on Mars and implications for a deep biosphere. *Nature Geoscience*, *6*(2), 133–138. https://doi.org/10.1038/ngeo1706

Michalski, J. R., Onstott, T. C., Mojzsis, S. J., Mustard, J., Chan, Q. H. S., Niles, P. B., & Johnson, S. S. (2018). The Martian subsurface as a potential window into the origin of life. *Nature Geoscience*, *11*(1), 21–26. https://doi.org/10.1038/s41561-017-0015-2

Murchie, S., Arvidson, R., Bedini, P., Beisser, K., Bibring, J. P., Bishop, J., et al. (2007). Compact reconnaissance Imaging Spectrometer for Mars (CRISM) on Mars Reconnaissance Orbiter (MRO). *Journal of Geophysical Research*, *112*, E05S03. https://doi.org/10.1029/2006JE002682

Mustard, J. F., Murchie, S. L., Pelkey, S. M., Ehlmann, B. L., Milliken, R. E., Grant, J. A., et al. (2008). Hydrated silicate minerals on Mars observed by the Mars Reconnaissance Orbiter CRISM instrument. *Nature*, *454*(7202), 305–309. https://doi.org/10.1038/nature07097

Noe Dobrea, E. Z., Bishop, J. L., McKeown, N. K., Fu, R., Rossi, C. M., Michalski, J. R., et al. (2010). Mineralogy and stratigraphy of phyllosilicate-bearing and dark mantling units in the greater Mawrth Vallis/west Arabia Terra area: Constraints on geological origin. *Journal of Geophysical Research*, *115*, E00D19. https://doi.org/10.1029/2009JE003351

Paul, D., Kumbhare, S. V., Mhatre, S. S., Chowdhury, S. P., Shetty, S. A., Marathe, N. P., et al. (2016). Exploration of microbial diversity and community structure of Lonar lake: The only hypersaline meteorite crater lake within basalt rock. *Frontiers in Microbiology*, *6*. https://doi.org/10.3389/fmicb.2015.01553

Pike, R. J. (1974). Ejecta from Large Craters on the Moon: Comments on the geometric model of McGetchin et al. *Earth and Planetary Science Letters*, *23*(3), 265–271. https://doi.org/10.1016/0012-821X(74)90114-9

Posamentier, H. W., & Kolla, V. (2003). Seismic geomorphology and stratigraphy of depositional elements in deep-water settings. *Journal of Sedimentary Research*, *73*(3), 367–388. https://doi.org/10.1306/111302730367

Poulet, F., Bibring, J. P., Mustard, J. F., Gendrin, A., Mangold, N., Langevin, Y., et al. (2005). Phyllosilicates on Mars and implications for early Martian climate. *Nature*, *438*(7068), 623–627. https://doi.org/10.1038/nature04274

Rasmussen, K. A., Johnson, T. C., & Romanovsky, V. V. (1998). Deep sediments of Lake Issyk-Kul, Kyrgyzstan; depositional history and evidence for central Asian paleoclimate change. In *Geological Society of America, 1998 annual meeting*.

Robertson, K. M., Milliken, R. E., & Li, S. (2016). Estimating mineral abundances of clay and gypsum mixtures using radiative transfer models applied to visible-near infrared reflectance spectra. *Icarus*, *277*, 171–186. https://doi.org/10.1016/j.icarus.2016.04.034

Rogers, A. D., & Aharonson, O. (2008). Mineralogical composition of sands in Meridiani Planum determined from Mars Exploration Rover data and comparison to orbital measurements. *Journal of Geophysical Research*, *113*, E06S14. https://doi.org/10.1029/2007JE002995

Rogers, A. D., & Christensen, P. R. (2007). Surface mineralogy of Martian low-albedo regions from MGS-TES data: Implications for upper crustal evolution and surface alteration. *Journal of Geophysical Research*, *112*, E01003. https://doi.org/10.1029/2006JE002727

Ruff, S. W., Christensen, P. R., Blaney, D. L., Farrand, W. H., Johnson, J. R., Michalski, J. R., et al. (2006). The rocks of Gusev crater as viewed by the Mini-TES instrument. *Journal of Geophysical Research*, *111*, E12S18. https://doi.org/10.1029/2006JE002747

Smith, M., Bandfield, J., & Christensen, P. (2000). Separation of atmospheric and surface spectral features in Mars Global Surveyor Thermal Emission Spectrometer (TES) spectra. *Journal of Geophysical Research*, *105*(E4), 9589–9607. https://doi.org/10.1029/1999JE001105

Stamnes, K., Tsay, S., & Istvan, L. (2000). DISORT, a general-purpose Fortran program for discrete-ordinate-method radiative transfer in scattering and emitting layered media: Documentation of methodology. *DISORT Report v1.1*. https://doi.org/10.1016/S0017-9310(02)00035-2

Valpola, S. E., & Ojala, A. E. K. (2006). Post-glacial sedimentation rate and patterns in six lakes of the Kokem??enjoki upper watercourse, Finland. *Boreal Environment Research*.

Viviano-Beck, C. E., Seelos, F. P., Murchie, S. L., Kahn, E. G., Seelos, K. D., Taylor, H. W., et al. (2014). Revised CRISM spectral parameters and summary products based on the currently detected mineral diversity on Mars. *Journal of Geophysical Research: Planets*, *119*, 1403–1431. https://doi.org/10.1002/2014JE004627

Wolff, M. J., Smith, M. D., Clancy, R. T., Arvidson, R., Kahre, M., Seelos, F., Murchie, S., et al. (2009). Wavelength dependence of dust aerosol single scattering albedo as observed by the Compact Reconnaissance Imaging Spectrometer. *Journal of Geophysical Research*, *114*, E00D04. https://doi.org/10.1029/2009JE003350

Wray, J. J., Milliken, R. E., Dundas, C. M., Swayze, G. A., Andrews-Hanna, J. C., Baldridge, A. M., et al. (2011). Columbus crater and other possible groundwater-fed paleolakes of Terra Sirenum, Mars. *Journal of Geophysical Research*, *116*, E01001 https://doi.org/10.1029/2010JE003694

Wright, S. P., Christensen, P. R., & Sharp, T. G. (2011). Laboratory thermal emission spectroscopy of shocked basalt from Lonar crater, India, and implications for Mars orbital and sample data. *Journal of Geophysical Research*, *116*, E09006 https://doi.org/10.1029/2010JE003785